

## V344 LYRAE: A TOUCHSTONE SU UMA CATAclySMIC VARIABLE IN THE KEPLER FIELD

MATT A. WOOD<sup>1</sup>, MARTIN D. STILL<sup>2,3</sup>, STEVE B. HOWELL<sup>4,2</sup>, JOHN K. CANNIZZO<sup>5,6</sup> ALAN P. SMALE<sup>7</sup>

*To appear in ApJ*

### ABSTRACT

We report on the analysis of the *Kepler* short-cadence (SC) light curve of V344 Lyr obtained during 2009 June 20 through 2010 Mar 19 (Q2–Q4). The system is an SU UMa star showing dwarf nova outbursts and superoutbursts, and promises to be a touchstone for CV studies for the foreseeable future. The system displays both positive and negative superhumps with periods of 2.20 and 2.06-hr, respectively, and we identify an orbital period of 2.11-hr. The positive superhumps have a maximum amplitude of  $\sim 0.25$ -mag, the negative superhumps a maximum amplitude of  $\sim 0.8$  mag, and the orbital period at quiescence has an amplitude of  $\sim 0.025$  mag. The quality of the *Kepler* data is such that we can test vigorously the models for accretion disk dynamics that have been emerging in the past several years. The SC data for V344 Lyr are consistent with the model that two physical sources yield positive superhumps: early in the superoutburst, the superhump signal is generated by viscous dissipation within the periodically flexing disk, but late in the superoutburst, the signal is generated as the accretion stream bright spot sweeps around the rim of the non-axisymmetric disk. The disk superhumps are roughly anti-phased with the stream/late superhumps. The V344 Lyr data also reveal negative superhumps arising from accretion onto a tilted disk precessing in the retrograde direction, and suggest that negative superhumps may appear during the decline of DN outbursts. The period of negative superhumps has a positive  $\dot{P}$  in between outbursts.

*Subject headings:* novae, cataclysmic variables; dwarf novae; stars: individual (V344 Lyr); white dwarfs; hydrodynamics

### 1. INTRODUCTION

Cataclysmic variable (CV) binary systems typically consist of low-mass main sequence stars that transfer mass through the L1 inner Lagrange point and onto a white dwarf primary via an accretion disk. Within the disk, viscosity acts to transport angular momentum outward in radius, allowing mass to move inward and accrete onto the primary white dwarf (e.g. Warner 1995a; Frank et al. 2002; Hellier 2001). In the case of steady-state accretion the disk is the brightest component of the system, with a disk luminosity  $L_{\text{disk}} \sim GM_1\dot{M}_1/R_1$ , where  $\dot{M}_1$  is the mass accretion rate onto a white dwarf of mass  $M_1$  and radius  $R_1$ .

While members of the novalike (NL) CV subclass display a nearly constant mean system luminosity, members of the dwarf nova (DN) subclass display quasi-periodic outbursts of a few magnitudes thought to arise from a thermal instability in the disk. Specifically, models suggest a heating wave rapidly transitions the disk to a hot, high-viscosity state which significantly enhances  $\dot{M}_1$  for

a few days. Furthermore, within the DN subclass there are the SU UMa systems that in addition to normal DN outbursts display superoutbursts which are up to a magnitude brighter and last a few times longer than the DN outbursts. The SU UMa stars are characterized by the appearance at superoutburst of periodic large-amplitude photometric signals (termed *positive superhumps*) with periods a few percent longer than the system orbital periods. So-called *negative* superhumps (with periods a few percent shorter than  $P_{\text{orb}}$ ) are also observed in some SU UMa systems.

The oscillation modes (i.e., eigenfrequencies) of any physical object are a direct function of the structure of that object, and thus an intensive study of SU UMa superhumps that can make use of both a nearly-ideal time-series data set as well as detailed three-dimensional high-resolution numerical models has the potential to eventually unlock many of the long-standing puzzles in accretion disk physics. For example, a fundamental question in astrophysical hydrodynamics is the nature of viscosity in differentially rotating plasma disks. It is typically thought to result from the magnetorotational instability (MRI) proposed by Balbus & Hawley (1998); Balbus (2003), but the observations to-date have been insufficient to test the model.

#### 1.1. V344 Lyrae

The *Kepler* field of view includes 12 CVs in the *Kepler* Input Catalog (KIC) that have published results at the time of this writing. Ten (10) of these systems are listed in Table 1 of Still et al. (2010, hereafter Paper I). Two additional systems have been announced since that publication, the dwarf nova system BOKS-45906 (KIC 9778689) (Feldmeier et al. 2011),

wood@fit.edu

<sup>1</sup>Department of Physics and Space Sciences, Florida Institute of Technology, Melbourne, FL 32901, USA

<sup>2</sup>NASA Ames Research Center, Moffett Field, CA 94095, USA

<sup>3</sup>Bay Area Environmental Research Institute, Inc., 560 Third St. West, Sonoma, CA 95476, USA

<sup>4</sup>National Optical Astronomy Observatory, Tucson, AZ 85719, USA

<sup>5</sup>CRESST and Astroparticle Physics Laboratory NASA/GSFC, Greenbelt, MD 20771, USA

<sup>6</sup>Department of Physics, University of Maryland, Baltimore County, 1000 Hilltop Circle, Baltimore, MD 21250, USA

<sup>7</sup>NASA/Goddard Space Flight Center, Greenbelt, MD 20771, USA

and the AM CVn star SDSS J190817.07+394036.4 (KIC 4547333) (Fontaine et al. 2011).

The star V344 Lyr (KIC 7659570) is a SU UMa star that lies in the *Kepler* field. Kato (1993) observed the star during a superoutburst ( $V \sim 14$ ), and reported the detection of superhumps with a period  $P = 2.1948 \pm 0.0005$  hr. In a later study Kato et al. (2002) reported that the DN outbursts have a recurrence timescale of  $16 \pm 3$  d, and that the superoutbursts have a recurrence timescale of  $\sim 110$  d. Ak et al. (2008) estimated a distance of 619 pc for the star using a period-luminosity relationship.

In Paper I we reported preliminary findings for V344 Lyr based on the second-quarter (Q2) *Kepler* observations, during which *Kepler* observed the star with a  $\sim 1$ -min cadence, obtaining over 123,000 photometric measurements. In that paper we reported on a periodic signal at quiescence that was either the orbital or negative superhump period, and the fact that the positive superhump signal persisted into quiescence and through the following dwarf nova outburst.

In Cannizzo et al. (2010, hereafter Paper II) we presented time-dependent modeling based on the accretion disk limit cycle model for the 270 d (Q2–Q4) light curve of V344 Lyr. We reported that the main decay of the superoutbursts is nearly perfectly exponential, decaying at a rate of  $\sim 12$  d  $\text{mag}^{-1}$ , and that the normal outbursts display a decay rate that is faster-than-exponential. In addition, we noted that the two superoutbursts are initiated by a normal outburst. Using the standard accretion disk limit cycle model, we were able to reproduce the main features of the outburst light curve of V344 Lyr. We significantly expand on this in Cannizzo et al. (2011) where we present the 1-year outburst properties of both V344 Lyr and V1504 Cyg (Cannizzo et al. 2011).

In this work, we report in detail on the results obtained by studying the *Kepler* Q2–Q4 data, which comprise without question the single-best data set obtained to-date from a cataclysmic variable star. The data set reveals signals from the orbital period as well as from positive and negative superhumps.

## 2. REVIEW OF SUPERHUMPS AND EXAMPLES

Before digging into the data, we briefly review the physical processes that lead to the photometric modulations termed superhumps.

### 2.1. Positive superhumps and the two-source model

The accretion disk of a typical dwarf nova CV that is in quiescence has a low disk viscosity and so inefficient exchange of angular momentum. As a result, the mass transfer rate  $\dot{M}_{L1}$  through the inner Lagrange point L1 is higher than the mass transfer rate  $\dot{M}_1$  onto the primary. Thus, mass accumulates in the disk until a critical surface density is reached at some annulus, and the fluid in that annulus transitions to a high-viscosity state (Cannizzo 1998; Cannizzo et al. 2010). This high-viscosity state propagates inward and/or outward in radius until the entire disk is in a high-viscosity state characterized by very efficient angular momentum and mass transport – the standard DN outburst (see, e.g., Cannizzo 1993a; Lasota 2001, for reviews). In this state,  $\dot{M}_1 > \dot{M}_{L1}$  and the disk drains mass onto the primary white dwarf.

During each DN outburst, however, the angular momentum transport acts to expand the outer disk radius slightly, and after a few to several of these, an otherwise normal DN outburst can expand the outer radius of the disk to the inner Lindblad resonance (near the 3:1 corotation resonance). This can only occur for systems with mass ratios  $q = M_2/M_1 \lesssim 0.35$  (Wood et al. 2009).

Once sufficient mass is present at the resonance radius, the common superhump oscillation mode can be driven to amplitudes that yield photometric oscillations. The superhump oscillation has a period  $P_+$  which is a few percent longer than the orbital period, where the *fractional period excess*  $\epsilon_+$  is defined as

$$\epsilon_+ \equiv \frac{P_+ - P_{\text{orb}}}{P_{\text{orb}}}. \quad (1)$$

These are the so-called *common* or *positive* superhumps, where the latter term reflects the sign of the period excess  $\epsilon_+$ . In addition to the SU UMa stars, positive superhumps have also been observed in novalike CVs (Patterson et al. 1993; Retter et al. 1997; Skillman et al. 1997; Patterson et al. 2005; Kim et al. 2009), the interacting binary white dwarf AM CVn stars (Patterson et al. 1993; Warner 1995b; Nelemans 2005; Roelofs et al. 2007; Fontaine et al. 2011), and in low-mass X-ray binaries (Charles et al. 1991; Mineshige et al. 1992; O’Donoghue & Charles 1996; Retter et al. 2002; Hynes et al. 2006).

Figure 1 shows snapshots from one full orbit of a smoothed particle hydrodynamics (SPH) simulation ( $q = 0.25$ , 100,000 particles) as well as the associated simulation light curve (see Simpson & Wood 1998; Wood & Burke 2007; Wood et al. 2009). The disk particles are color-coded by the change in internal energy over the previous timestep, and the Roche lobes and positions of  $M_1$  are also shown. Panels 1 and 6 of Figure 1 shows the geometry of the disk at superhump maximum. Note that here the superhump light source is viscous dissipation resulting from the compression of the disk opposite the secondary star. The local density and shear in this region are both high, leading to enhanced viscous dissipation in the strongly convergent flows. The orbit sampled in the Figure is characteristic of early superhumps where the disk oscillation mode is saturated, and the resulting amplitude significantly higher ( $\sim 0.15$  mag) than the models produce when dynamical equilibrium ( $\sim 0.03$  mag) due to the lower mean energy production in the models at superhump onset.

As a further detail, we note that whereas the 2 spiral dissipation waves are stationary in the co-rotating frame before the onset of the superhump oscillation, once the oscillation begins, the spiral arms advance in the prograde direction by  $\sim 180^\circ$  in the co-rotating frame during each superhump cycle. This prograde advancement can be seen by careful inspection of the panels in Figure 1. Indeed, this motion of the spiral dissipation waves is central to the superhump oscillation – a spiral arm is “cast” outward as it rotates through the tidal field of the secondary, and then brightens shortly afterward as it compresses back into the disk in a converging flow (Smith et al. 2007; Wood et al. 2009).

While viscous dissipation within the periodically-flexing disk provides the dominant source of the super-

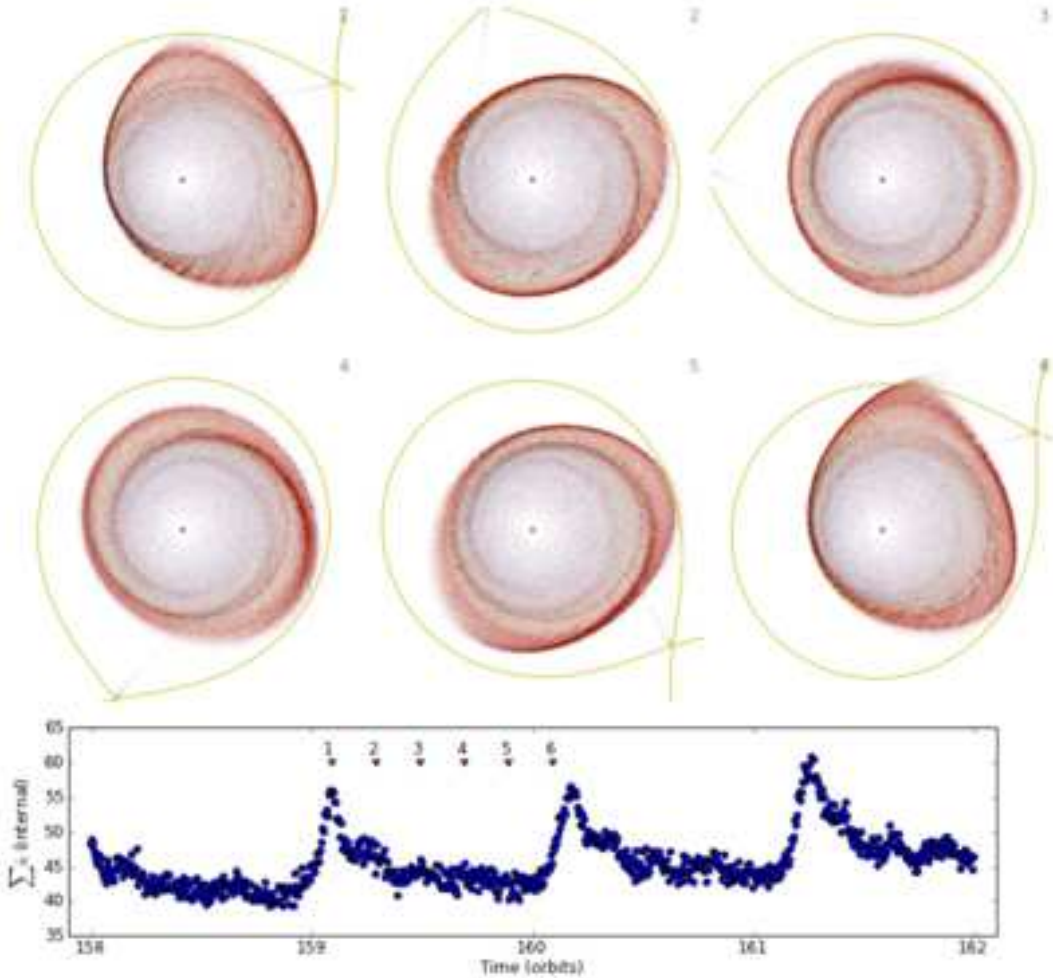


FIG. 1.— Snapshots from one orbit of a  $q = 0.25$  SPH accretion disk simulation shortly after superhump onset. The 100,000 simulation particles are color-coded by their internal energy change (“luminosity”) over the previous simulation time step. The simulation light curve shown is calculated as the sum of the luminosities of all the particles. Note that superhump maximum corresponds to frames 1 and 6, where the disk opposite the secondary is radially compressed and hence a region of strongly convergent flows. Note also that the accretion stream impact region is deeper in the potential well in frame 3 than in frames 1 and 6 – this yields the “late” superhump signal.

hump modulation, the accretion stream bright spot also provides a periodic photometric signal when sweeping around the rim of a non-axisymmetric disk (Vogt 1982; Osaki 1985; Whitehurst 1988; Kunze 2004). The bright spot will be most luminous when it impacts most deeply in the potential well of the primary (e.g., panel 3 of Figure 1, and fainter when it impacts the rim further from the white dwarf primary (Panels 1 and 6). This signal is swamped by the superhumps generated by the flexing disk early in the superoutburst, but dominates once the disk is significantly drained of matter and returns to low state. The disk will continue to oscillate although the driving is much diminished, and thus the stream mechanism will continue to yield a periodic photometric signal of decreasing amplitude until the oscillations cease completely.

This photometric signal is what is termed *late su-*

*perhumps* in the literature (e.g., Hessman et al. 1992; Patterson et al. 2000, 2002a; Templeton et al. 2006; Sterken et al. 2007; Kato et al. 2009, 2010). Rolfe et al. (2001) presented a detailed study of the deeply eclipsing dwarf nova IY UMa observed during the late superhump phase where they found exactly this behavior. They used the shadow method Wood et al. (1986) to determine the radial location of the bright spot (disk edge) in 22 eclipses observed using time-series photometry. They found that the disk was elliptical and precessing slowly at the beat frequency of the orbital and superhump frequencies, and that the brightness of the stream-disk impact region varied as the square of the relative velocity of the stream and disk material (see also Smak 2010). Put another way, the bright spot was brighter when it was located on the periastron quadrant of the elliptical disk, and fainter on the apastron quadrant.

Thus, two distinct physical mechanisms give rise to positive superhumps: viscous dissipation in the flexing disk, driven by the resonance with the tidal field of the secondary, and the time-variable viscous dissipation of the bright spot as it sweeps around the rim of a non-axisymmetric disk<sup>8</sup>. For the remainder of this paper we refer to this as the *two-source model of positive superhumps* (see also Kunze 2002, 2004). These two signals are approximately antiphased, and in systems where both operate at roughly equal amplitude, the Fourier transform of the light curve can show a larger amplitude for the second harmonic (first overtone) than for the fundamental (first harmonic).

As an example of this double humped light curve, in Figure 2 we show 20 orbits of the  $q = 0.25$  simulation discussed above (Figure 1) starting at orbit 400, by which time the system had settled into a state of dynamical equilibrium. The inset in this Figure shows the average superhump pulse shape obtained from orbits 400-500 of the simulation, where we have set phase zero to primary minimum. Note that here the average pulse shape is complex but approximately double-peaked. The Fourier transform displays maximum power at twice the fundamental frequency. When we examine the disk profiles, we find that the dominant peak arises from the disk superhump described above, but the secondary peak roughly half a cycle later results from the impact of the bright spot deeper in the potential well of the primary (see panel 4 of Figure 1). The substructure of this secondary maximum results from the interaction of the accretion stream with the spiral arm structures that advance progradely in the co-rotating frame. Panel 3 of Figure 1 is representative of the disk structure at the time of the the small dip in brightness observed at superhump phase 0.55. The dip is explained by the fact that the accretion stream bright spot at this phase is located in the low-density inter-arm region, and therefore that the accretion stream can dissipate its energy over a longer distance. In addition the oscillating disk geometry results in this region having a larger radius, and lower velocity contrast near this phase. Howell et al. (1996) discuss the observation and phase evolution of the two secondary humps in the SU UMa system TV Corvi.

The 3 AM CVn (helium CV) systems that are in permanent high state – AM CVn (Skillman et al. 1999), HP Lib (Patterson et al. 2002a) and the system SDSS J190817.07+394036.4 (KIC 004547333) announced recently by Fontaine et al. (2011) – all display average pulse shapes that are strongly double humped. AM CVn itself is frequently observed to show no power in the Fourier transform at the fundamental superhump oscillation frequency (Smak 1967; Faulkner et al. 1972; Patterson et al. 1992; Skillman et al. 1999). AM CVn systems are known to be helium mass transfer systems with orbital periods ranging between 5 min and  $\sim 1$  hr (see reviews by Warner 1995b; Solheim 2010).

In contrast, the hydrogen-rich old-novae and novalike

<sup>8</sup> For completeness, we note that recently Smak (2009, 2011) has proposed that the standard model, described above, does not explain the physical source of observed superhump oscillations. Instead, he suggests that irradiation on the face of the secondary is modulated, which yields a modulated mass transfer rate  $\dot{M}_{L1}$ , which in turn results in modulated dissipation of the kinetic energy of the stream.

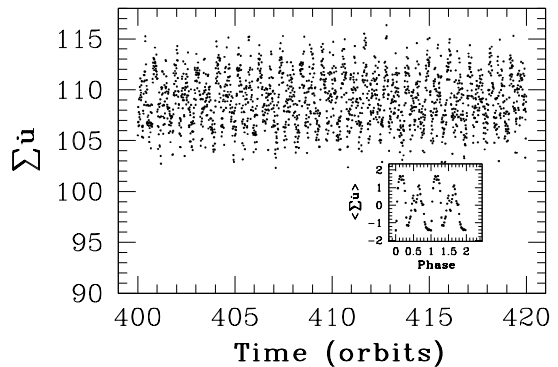


FIG. 2.— Twenty orbits of the simulation light curve once the dynamical equilibrium state has been reached in the  $q = 0.25$  simulation discussed above. The light curve is double humped. The inset shows the average light curve calculated from orbits 400 to 500, with the phase set to zero for primary minimum. Primary maximum again corresponds to modulation in the disk as discussed. Secondary maximum is caused by the accretion stream impact spot hitting minimum radius of the non-axisymmetric disk. The substructure of the secondary maximum is discussed in the text.

CVs that show permanent superhumps display mean pulse shapes that are nearly always similar to the saturation phase light curves as shown in Figure 1, and there is no example we know of where a permanent superhump system shows a strong double-humped light curve. The reason for this is clear upon reflection: the AM CVn disks are physically much smaller than the disks in systems with hydrogen-rich secondary stars, resulting in a much higher specific kinetic energy to be dissipated at the bright spot since the disk rim is much deeper in the potential well of the primary. The smaller disk may also yield a smaller amplitude for the disk oscillation signal. In the hydrogen-rich systems in permanent outburst, the disks are large, the mass transfer rates are high, and the disk signal dominates, with a relatively minor contribution from the stream source.

We tested the viability of the two-source model through three additional numerical experiments. First, we again restarted the above simulation at orbit 400, but now with the accretion flow through L1 shut off completely. In this run, there is no accretion stream and hence no bright spot contribution. We show the first 20 orbits of the simulation light curve in Figure 3. With the stream present, the light curve has the double-humped shape of Figure 2 above, but without the stream the light curve is sharply peaked with no hint of a double hump. Note that because there is no low-specific-angular-momentum material accreting at the edge of the disk, the disk can expand further into the driving zone. This expansion results in the pulse shape growing in amplitude as the mean disk luminosity drops. The pulse shape averaged over orbits 410-440 is shown as an inset in the Figure, and clearly shows that the oscillating disk is the only source of modulation in the light curve – maximum brightness corresponds to a disk geometry like that from panel 1 of Figure 1 above. The mean brightness is roughly constant for orbits 410-440, and at orbit 440 the mean brightness and pulse amplitude begin to decline as some 50% of the initially-present SPH disk particles are accreted by orbit 450.

Our second test was to restart the simulation a third time at orbit 400, but this time to enhance the injec-

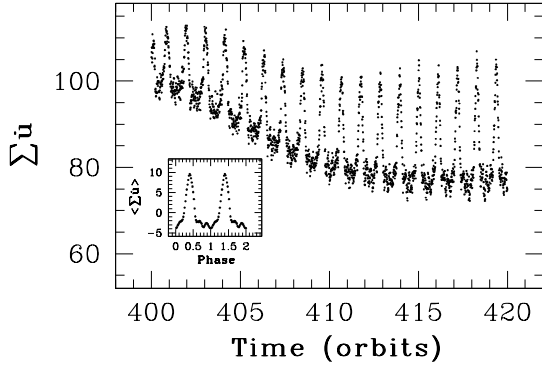


FIG. 3.— The first 20 orbits after SPH simulation restart with no mass flow through L1. The pulse shape increases in amplitude as the mean luminosity increases, resulting from the expansion of the disk. Note that the pulse shape is strongly – and singly – peaked. The mean pulse shape calculated over orbits 410–440 is shown in the inset.

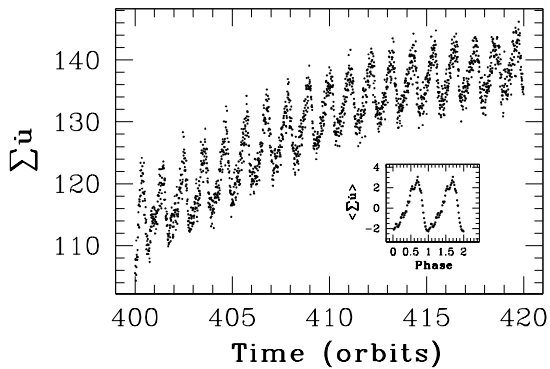


FIG. 4.— The first 20 orbits after SPH simulation restart with enhanced mass flow through L1 as described in the text. The pulse shape is saw-toothed, and maximum light corresponds to the phase where the bright spot is deepest in the potential well of the non-axisymmetric flexing disk. The average pulse shape over these 20 orbits is shown as an inset. The mean system luminosity increased with the simulation particle count. The mean pulse shape calculated over orbits 410–440 is shown in the inset.

tion rate of SPH particles (mass flow) at L1 by roughly a factor of 2 over that required to keep the disk particle count constant (Figure 4). This enhanced mass flux again dramatically changes the character of the light curve. Here the mean pulse shape as shown in the inset is saw-toothed, but with the substructure near the peak from the interaction of the stream with the periodic motion of the spiral features in the disk as viewed in the co-rotating frame. Careful comparison of the times of maximum in these two runs (Figures 3 and 4) reveals that they are antiphased with each other. For example, the simulation light curve in Figure 3 shows maxima at times of 403.0 and 404.0 orbits, whereas the simulation light curve in Figure 4 shows minima at these same times.

Our third experiment was more crude, but still effective. We began with a disk from a  $q = 0.2$  low-viscosity SPH simulation run that was in a stable, non-oscillating state. We offset all of the the SPH particles an amount  $0.03a$  along the line of centers [i.e.,  $(x, y, z) \rightarrow (x + 0.03a, y, z)$ ], scaled the SPH particle speeds (but not directions) using the *vis viva* equation

$$v^2 = GM_1 \left( \frac{2}{r} - \frac{1}{a} \right), \quad (2)$$

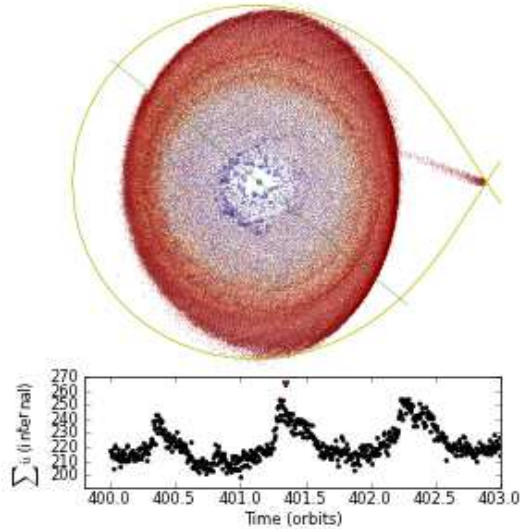


FIG. 5.— A snapshot at orbit 401.35 from a  $q = 0.40$  SPH simulation showing negative superhumps. The green line running diagonally though the primary indicates the location of the line of nodes; the disk midplane includes this line, but is below the orbital plane to the right of the line, and above the orbital plane to the left of the line. The particles are color coded by luminosity, and the brightest are rendered larger. It can be seen that the accretion stream impact region at this phase is deep in the potential well of the primary, roughly at the line of nodes. The deeper the accretion stream impact region, the brighter the bright spot. The simulation light curve is derived from the “surface” particles calculated using a simply ray-trace technique.

and restarted the simulation. This technique gives us disk which is non-axisymmetric but not undergoing the superhump oscillation. The results were as expected: we find maxima in the simulation light curves at the phases where the accretion stream impacts the disk edge deepest in the potential well of the primary.

In summary, numerical simulations reproduce the two-source model for positive superhumps.

## 2.2. Negative Superhumps

Photometric signals with periods a few percent shorter than  $P_{\text{orb}}$  have also been observed in several DN, novae-like, and AM CVn systems – in some cases simultaneously with positive superhumps (see, e.g., Table 2 of Wood et al. 2009, and Woudt et al. 2009). These oscillations have been termed *negative* superhumps owing to the sign of the period “excess” obtained using Equation 1. The system TV Col was the first system to show this signal, and Bonnet-Bidaud et al. (1985) suggested that the periods were consistent with what would be expected for a disk that was tilted out of the orbital plane and freely precessing with a period of  $\sim 4$  d. Barrett et al. (1988) expanded on this and suggested what is now the accepted model for the origin of negative superhumps: the transit of the accretion stream impact point across the face of a tilted accretion disk that precesses in the retrograde direction (see Wood et al. 2000; Wood & Burke 2007; Wood et al. 2009; Foulkes et al. 2006). As in the stream source for positive superhumps, the modulation results because the accretion stream impact point has a periodically-varying depth in the potential well of the primary star.

Finding the term “negative period excess” unnecessarily turgid, in this work we refer to the *period deficit*  $\epsilon_-$

defined as

$$\epsilon_- \equiv \frac{P_{\text{orb}} - P_-}{P_{\text{orb}}}. \quad (3)$$

Empirically, it is found that for systems showing both positive and negative superhumps that  $\epsilon_+/\epsilon_- \sim 2$  (Patterson 1999; Retter et al. 2002).

We show in Figure 5 a snapshot from a  $q = 0.40$  simulation that demonstrates the physical origin of negative superhumps. At orbit 400, the disk particles were tilted  $5^\circ$  about the  $x$ -axis and the simulation restarted. The green line in the Figure running diagonally through the primary indicates the location of the line of nodes; the disk mid-plane includes this line, but is below the orbital plane to the right of the line, and above the orbital plane to the left of the line. The disk particles are again color-coded by luminosity, and the brightest particles are shown with larger symbols. The ballistic accretion stream can be followed from the L1 point to the impact point near the line of nodes. The simulation light curve is derived from the “surface” particles as described in Wood & Burke (2007). The times of maximum of the negative superhump light curve occur when accretion stream impact point is deepest in the potential of the primary and on the side of the disk facing the observer. A second observer viewing the disk from the opposite side would still see negative superhumps, but antiphased to those of the first.

Having introduced a viable model for positive superhumps and their evolution, let us now compare the model to the *Kepler* V344 Lyr photometry.

### 3. *Kepler* PHOTOMETRIC OBSERVATIONS

The primary science mission of the NASA Discovery mission *Kepler* is to discover and characterize terrestrial planets in the habitable zone of Sun-like stars using the transit method (Borucki et al. 2010; Haas et al. 2010). The spacecraft is in an Earth-trailing orbit, allowing it to view its roughly 150,000 target stars continuously for the 3.5-yr mission lifetime. The photometer has no shutter and stares continuously at the target field. Each integration lasts 6.54 s. Due to memory and bandwidth constraints, only data from the pre-selected target apertures are kept. *Kepler* can observe up to 170,000 targets using the long-cadence (LC) mode, summing 270 integrations over 29.4 min, and up to 512 targets in the short-cadence (SC) mode, summing 9 integrations for an effective exposure time of 58.8 s.

There are gaps in the *Kepler* data streams resulting from, for example, monthly data downloads using the high-gain antenna and quarterly  $90^\circ$  spacecraft rolls, as well as unplanned safe-mode and loss of fine point events. For further details of the spacecraft commissioning, target tables, data collection and processing, and performance metrics, see Haas et al. (2010), Koch et al. (2010), and Caldwell et al. (2010).

*Kepler* data are provided as quarterly FITS files by the Science Operations Center after being processed through the standard data reduction pipeline (Jenkins et al. 2010). The raw data are first corrected for bias, smear induced by the shutterless readout, and sky background. Time series are extracted using simple aperture photometry (SAP) using an optimal aperture for each star, and these “SAP light curves” are what we use in this study. The dates and times for the beginning and end of Q2,

Q3 and Q4 are listed in Table 1.

The full SAP light curve for *Kepler* quarters Q2, Q3, and Q4 is shown in flux units in Figure 6. In Figure 2 of Paper II we show the full SAP light curve in Kp magnitude units. As noted in Paper II and evident in Figure 6, the superoutbursts begin as normal DN outbursts.

The Q2 data begin at BJD 2455002.5098. For simplicity we will below refer to events as occurring on, for example, day 70, which should be interpreted to mean BJD 2455070 – that is we take BJD 2455000 to be our fiducial time reference.

In this paper, we focus on the superhump and orbital signals present in the data. The outburst behavior of these data in the context of constraining the thermal-viscous limit cycle is published separately (Paper II).

To remove the large-amplitude outburst behavior from the raw light curve – i.e., to high-pass filter the data – we subtracted a boxcar-smoothed copy of the light curve from the SAP light curve. The window width was taken to be the superhump cycle length (2.2 hr or 135 points). To minimize the effects of data gaps, we split the data into a separate file anytime we had a data gap of more than 1 cycle. This resulted in 10 data chunks. Once the data residual light curve was calculated, we again recombined the data into a single file. The results for Q2, Q3, and Q4 are shown in Figures 7, 8, and 9, respectively.

We also calculated the fractional amplitude light curve by dividing the raw light curve by the smoothed light curve, and subtracting 1.0. However, as expected, the amplitudes of the photometric signals in the residual light curve are more nearly constant than those in the fractional amplitude light curve. This is because the superhump signals – both positive and negative – have amplitudes determined by physical processes within the disk that are not strong functions of the overall disk luminosity.

### 4. THE FOURIER TRANSFORM

In Figure 10 we show the discrete Fourier transform amplitude spectra for the current data set. We took the transforms over 2000 frequency points spanning 0 to 70 cycles per day. Each transform is of a 5 day window of the data, and the window was moved roughly 1/2 day between subsequent transforms. The color scale indicates the logarithm of the residual count light curve amplitude in units of counts per cadence. In Figure 11 we show a magnified view including only frequencies 9.5 to 12.5 c/d to better bring out the 3 fundamental frequencies in the system.

Figures 10 and 11 are rich with information. The positive superhumps ( $P_+ = 2.20$  hr) dominate the power for days  $\sim 58$ –80 and  $\sim 162$ –190. In Figure 11 we see that the time evolution of the fundamental oscillation frequency is remarkably similar in both superoutbursts. The dynamics behind this are discussed below in §5.2 where the O-C diagrams are presented.

Once the majority of the mass that will accrete during the event has done so, the disk transitions back to the low state. This occurs roughly 15 d after superhump onset for V344 Lyr. During this transition, the disk source of the superhump modulation fades with the disk itself, and the stream source of the superhump modulation begins to dominate. A careful inspection of Figure 10 shows that at this time of transition between disk and stream



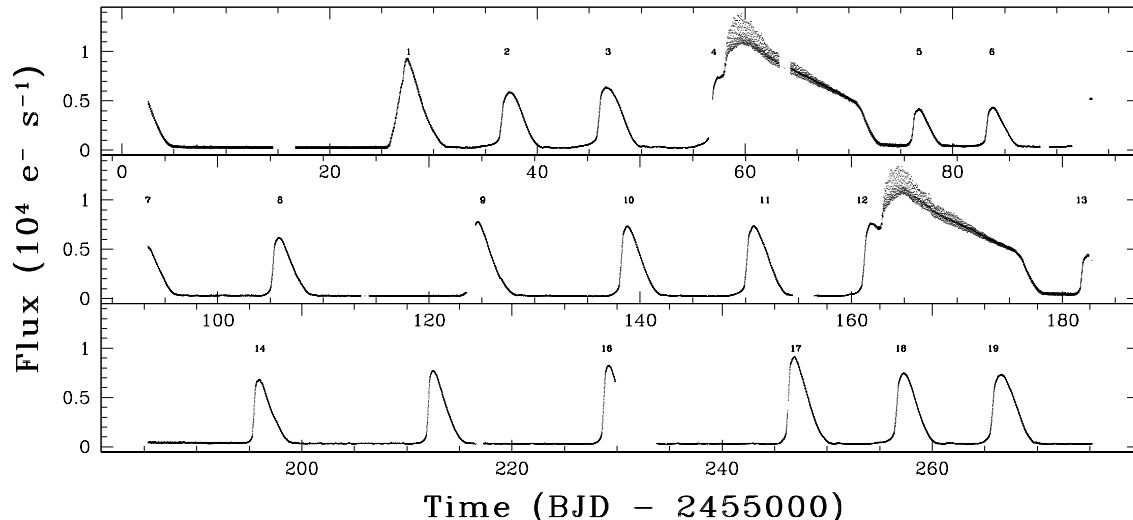


FIG. 6.— The *Kepler* Q2, Q3, and Q4 light curve of V344 Lyr in flux units. The outbursts are labeled 1 to 19.

TABLE 1  
JOURNAL OF OBSERVATIONS

Quarter	MJD	Start <sup>a</sup> UT	MJD	End <sup>b</sup> UT
Q2	55002.008	2009 Jun 20 00:11	55090.975	2009 Sep 17 11:26
Q3	55092.712	2009 Sep 18 17:05	55182.007	2009 Dec 17 00:09
Q4	55184.868	2009 Dec 19 20:49	55274.714	2010 Mar 19 17:07

<sup>a</sup> The start MJD and UT dates are the mid-point of the first cadence of the SC time series for each quarter.

<sup>b</sup> The end MJD and UT dates are the mid-point of the last cadence of the SC time series for each quarter.

superhumps, there is comparable power in the second harmonic (first overtone) as found in the fundamental. The behavior of the light curve and Fourier transform are more clearly displayed in Figure 12 which shows 2 days of the light curve during the transition period, and the associated Fourier transforms. In both cases, the “knee” in the superoutburst light curve (see Figure 6 occurs just past the midpoint of the data sets. Although the second harmonic is strong in transition phase, the pulse shape of the disk superhump signal is sharply peaked so the fundamental remains prominent in the Fourier transform (see Figure 12).

As can clearly be seen in Figure 11, the orbital period of 2.10 hr (11.4 c/d) only becomes readily apparent in the Q4 data, starting at about day 200, and it dominates the Q4 Fourier transforms. Once identified in Q4, the orbital frequency appears to show some power in the week before the first superoutburst in Q2, and between days  $\sim 130$  and the second superoutburst in Q3. Note, however, that the amplitude of the orbital signal is roughly 1 order of magnitude smaller than the amplitude of the negative superhump signal, and as much as 2 orders of magnitude smaller than the amplitude of the positive superhump signal. In these data, the orbital signal is found only when the positive or negative superhump signals are weak or absent. We discuss the physical reason for this below.

Finally, we note that we searched the Fourier transform of our *Kepler* short-cadence (SC) data out to the Nyquist

frequency of 8.496 mHz for any significant high frequency power which might for example indicate accretion onto a spinning magnetic primary star (i.e., intermediate polar or DQ Her behavior). We found no reliable detection of higher frequencies in the data, beyond the well-known spurious frequencies present in *Kepler* time series data at multiples of the LC frequency ( $n \times 0.566427$  mHz =  $48.9393$  c d<sup>-1</sup> Gilliland et al. 2010). For a full list of possible spurious frequencies in the SC data, see the *Kepler Data Characteristics Handbook*.

#### 4.1. The Orbital Period

The orbital period is the most fundamental clock in a binary system. In the original Q2 data presented by Still et al. (2010), the only frequencies that were clearly present in the data were the 2.20-hr (10.9 c/d) superhump period and the period observed at 2.06-hr (11.7 c/d). In Paper I we identified this latter signal as the orbital period but discussed the possibility that it is a negative superhump period. The Q3 data revealed a marginal detection of a period of 2.11 hr (11.4 c/d), and this period is found to dominate the Q4 data (see Figure 13). The average pulse shape for this signal averaged over days 200-275 is shown in Figure 14. We can now safely identify this 2.11 hr (11.4 c/d) signal as the system orbital period, which then indicates that the 2.06 hr (11.7 c/d) signal is a negative superhump.

The orbital period was determined using the method

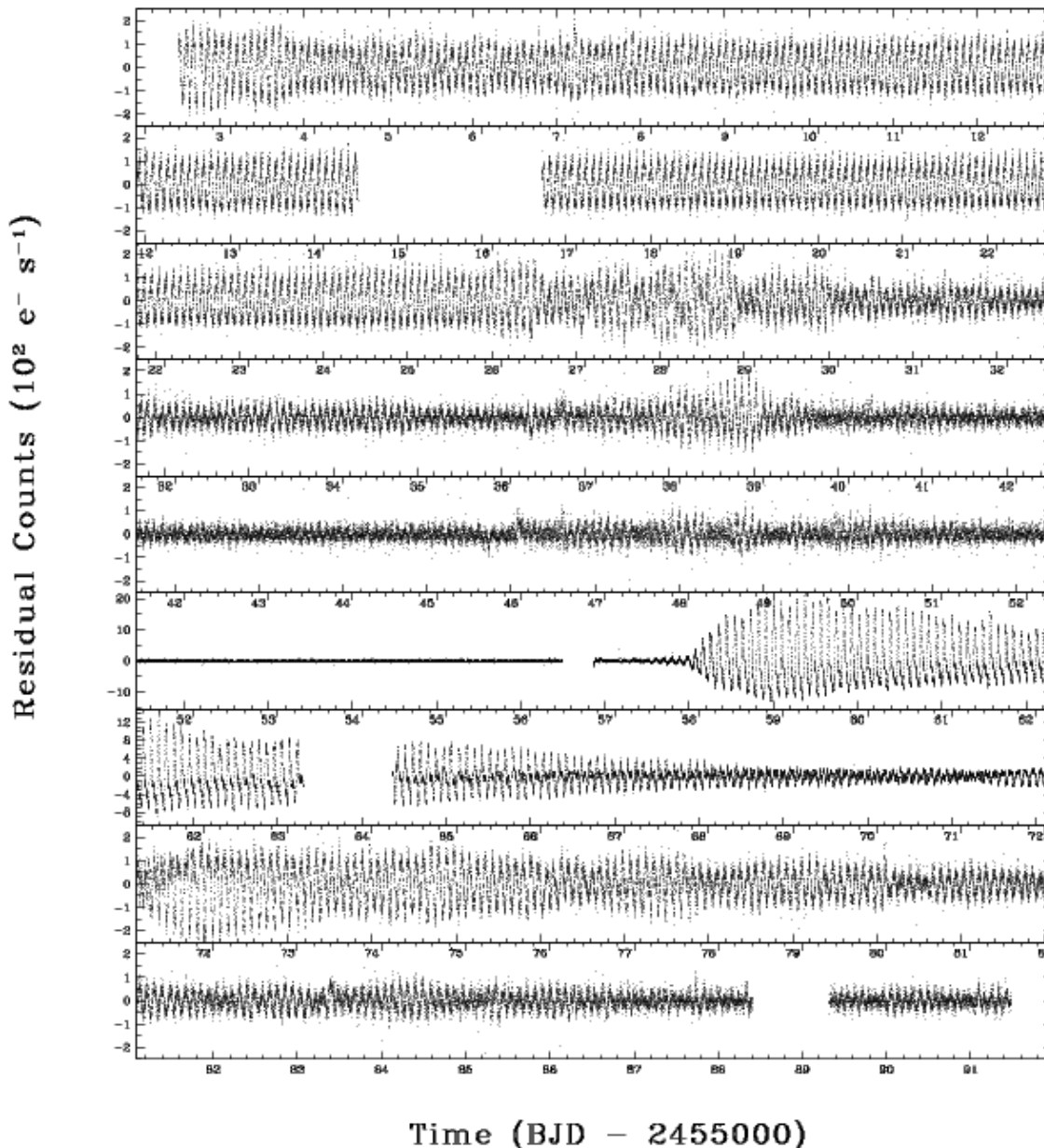


FIG. 7.— The residuals of the *Kepler* Q2 V344 Lyr light curve after subtraction of a smoothed copy of the SAP light curve. Each panel shows approximately 10 days of data ( $\sim 120$  cycles). Note that the vertical scaling of the 2 panels showing the high-amplitude positive superhumps ( $P_+ = 2.20$  hr,  $\nu_+ = 10.9$  c d $^{-1}$ ) differ from the rest (days  $\sim 52$ -72), and that there is a small amount of overlap between panels. The negative superhump signal dominates in days  $\sim 2$ -40 ( $P_- = 2.06$  hr period,  $\nu_- = 11.7$  c d $^{-1}$ ). The positive superhumps dominate the power for days  $\sim 58$  through the end of the quarter.

of non-linear least squares fitting a function of the form

$$y(t) = A \sin[2\pi(t - T_0)/P]. \quad (4)$$

The results of the fit are

$$\begin{aligned} P &= 0.087904 \pm 3 \times 10^{-6} \text{ d}, \\ &= 2.109696 \pm 7 \times 10^{-5} \text{ hr}, \\ T_0 &= \text{BJD } 2455200.2080 \pm 0.0006, \\ A &= 7.8 \pm 0.1 \text{ e}^- \text{ s}^{-1}. \end{aligned}$$

Note that the amplitude is only roughly 25 mmag – an order of magnitude or more smaller than the peak amplitudes of the positive and negative superhumps in the system.

That an orbital signal exists indicates that the system is not face-on. The source of the orbital signal of a non-superhumping CV can be either the variable flux along the line of site from a bright spot that is periodically shadowed as it sweeps around the back rim of the disk, or the so-called reflection effect as the face of the secondary star that is illuminated by the UV radiation of the disk rotates in to and out of view (e.g., Warner 1995a). In Figure 11, we find that the orbital signal is never observed when the positive superhumps are present, but this is not a strong constraint as the positive superhump amplitude swamps that of the orbital signal.

More revealing is the interplay between the orbital signal, the negative superhump signal, and the DN out-



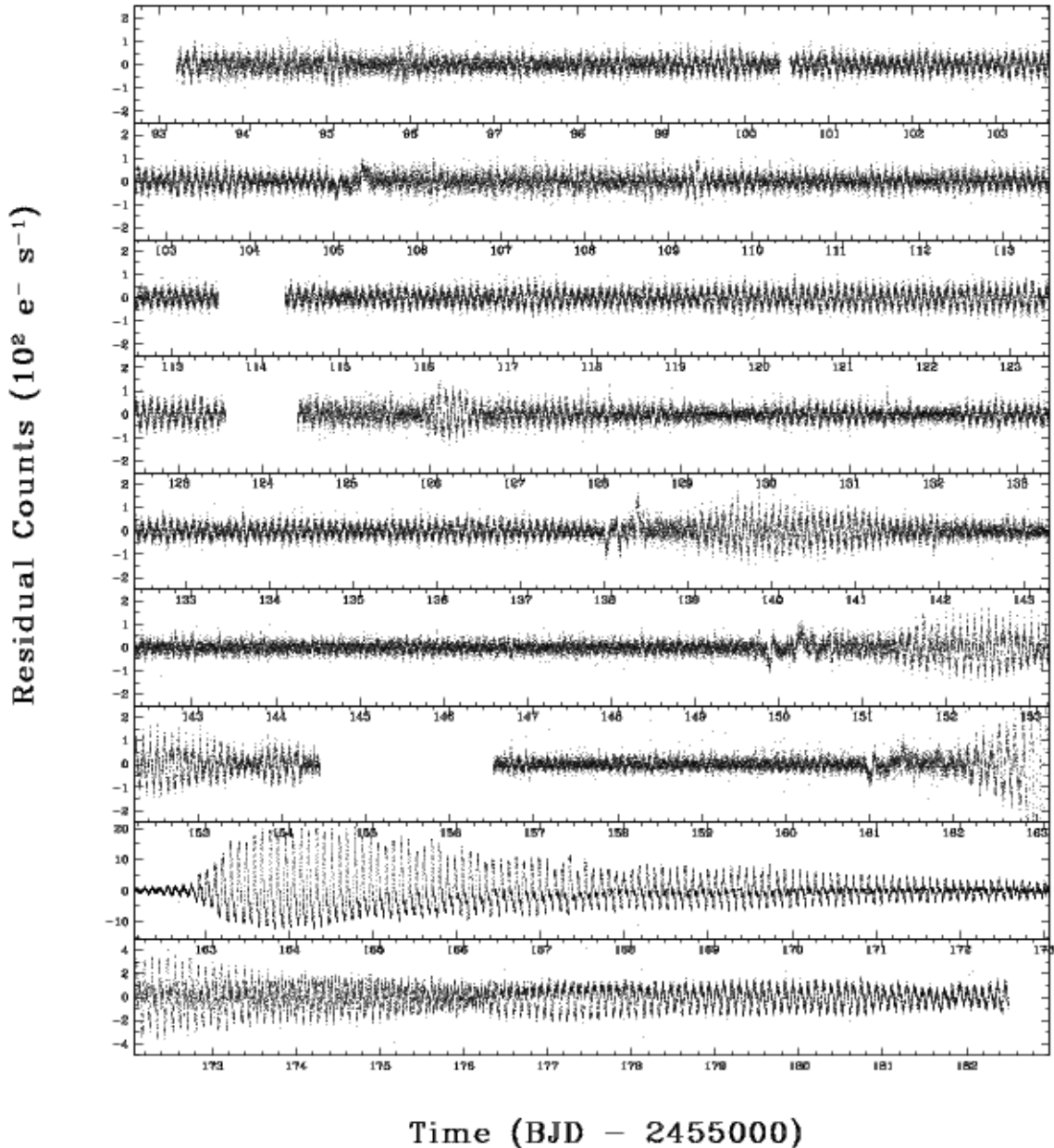


FIG. 8.— The residuals of the *Kepler* Q3 V344 Lyr light curve. The positive superhumps dominate the power for days  $\sim 162$  through the end of the quarter. The negative superhumps dominate the signal during days  $\sim 100$ -160. The vertical scaling of the bottom 2 panels differs from the rest. The features that appear during days  $\sim 105$ , 138, 150, and 161 are artifacts of the reduction process.

bursts. In Q2 and Q3, the orbital signal appears only when the negative superhump signal is weak or absent. This is consistent with the idea that the addition of material from the accretion stream should bring the disk back to the orbital plane roughly on the mass-replacement time scale (Wood & Burke 2007; Wood et al. 2009). The strong negative superhump signal early in Q2 indicates a tilt of  $\sim 5^\circ$ , sufficient for the accretion stream to avoid interaction with the disk rim for all phases except those in which the disk rim is along the line of nodes. As the disk tilt declines, however, an increasing fraction of the stream material will impact the disk rim and not the inner disk – in other words, the orbital signal will grow at the expense of the negative superhump signal. This appears to be consistent with the data in hand and if

so would suggest that the orbital signal results from the bright spot in V344 Lyr, but the result is only speculative at present.

In Figure 15 we show the O-C phase diagram for  $P_{\text{orb}}$ . We fit 20 cycles for each point in the Figure, and moved the window 10 cycles between fits. The small apparent wanderings in phase result from interference from the other periods present, and also appear to correlate with the outbursts. We show the 2D DFT for days 200 to 275 in Figure 16. Here we used a window width of 2 days, and shifted the window by 1/8th of a day between transforms. We show amplitude per cadence. The orbital signal appears to be increasing in amplitude slightly during Q4, perhaps as a result of the buildup of mass in the outer disk after several DN outbursts. The large amplitudes

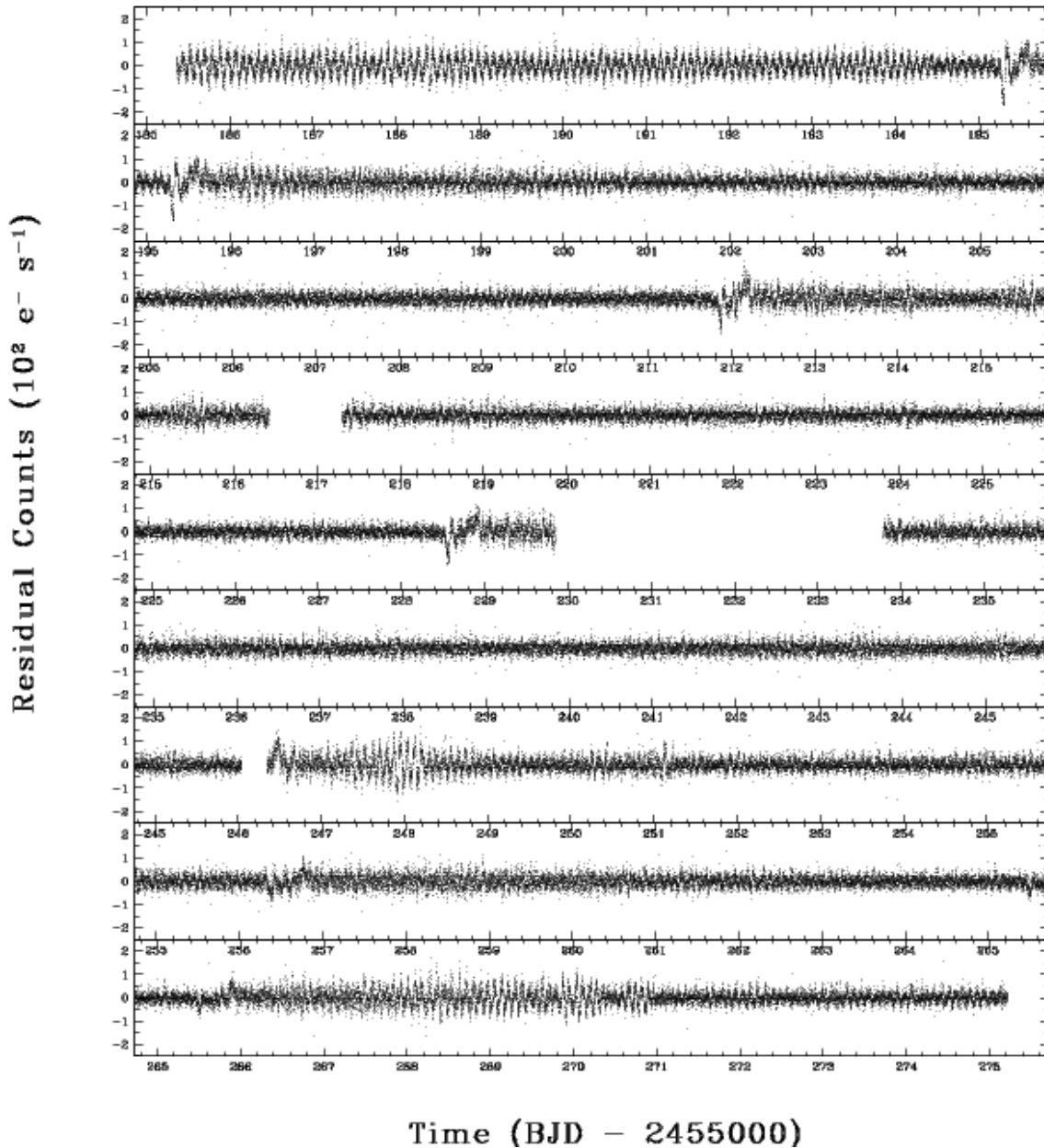


FIG. 9.— The residuals of the *Kepler* Q4 V344 Lyr light curve. The orbital signal ( $P_{\text{orb}} = 2.11$  hr,  $\nu_{\text{orb}} = 11.4$  c d $^{-1}$ ) dominates following the decay of the positive superhump signal at day  $\sim 190$ . The features that appear during days  $\sim 195$ , 212, 228, 246, and 256 are artifacts of the reduction process.

found for the orbital signal in Figure 15 during outbursts 17 and 19 (starting days  $\sim 246.5$  and 266, respectively) are spurious, resulting from the higher-frequency signals found on the decline from maximum in each case. As discussed below, outbursts 17 and 19 both show evidence for triggering a negative superhump signal, and the light curve for outburst 19 yields a complex Fourier transform that shows power at the orbital frequency, the negative superhump frequency, and at 12.3 c/d (1.95 hr).

#### 4.2. Observed Positive Superhumps

The light curve for V344 Lyr is rich in detail, and in particular provides the best data yet for exploring the time evolution of positive superhumps. As discussed above, the superhumps are first driven to resonance during the DN outburst that precedes the superoutburst as

the heating wave transitions the outer disk to the high-viscosity state allowing the resonance to be driven to amplitudes that can modulate the system luminosity. Close inspection of the positive superhumps in Figures 7 and 8 shows that in both cases the amplitude of the superhump is initially quite small, but grows to saturation ( $A \sim 0.25$  mag) in roughly 16 cycles. There is a signal evident preceding the second superoutburst (days  $\sim 156.5$  to 161) – this is a blend of the orbital signal and a very weak negative superhump signal.

The mean superhump period obtained by averaging the results from non-linear least squares fits to the disk superhump signal during the two superoutburst growth through plateau phases is  $P_+ = 0.091769(3)$  d = 2.20245(8)hr. The errors quoted for the last signifi-

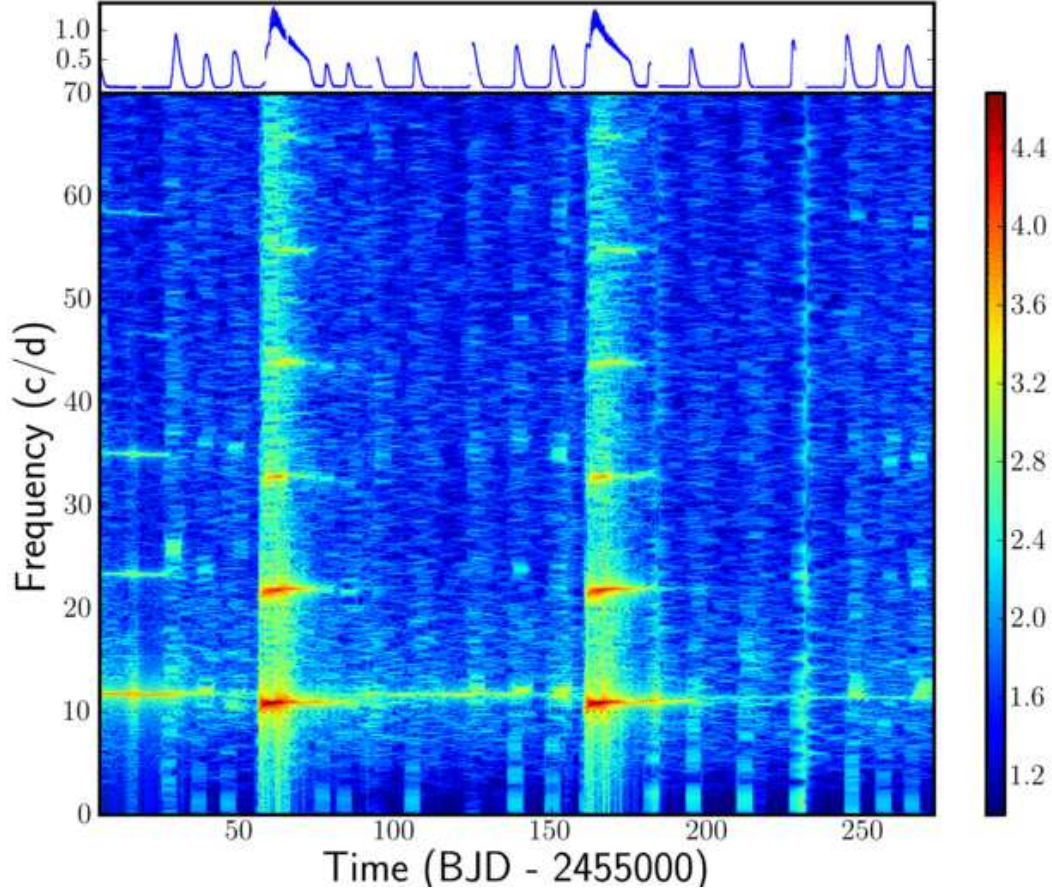


FIG. 10.— The 2D DFT of the Kepler Data from Q2, Q3, and Q4. Shown here is the logarithm of the amplitude versus time and frequency. There are three fundamental periods visible, plus higher harmonics of two of these. The positive superhumps ( $P_+ = 2.20$  hr,  $\nu_+ = 10.9$  c d $^{-1}$ ) dominate the power for days  $\sim 58$ –80 and  $\sim 162$ –190. The negative superhumps dominate the signal during days  $\sim 100$ –160 ( $P_- = 2.06$  hr,  $\nu_- = 11.7$  c d $^{-1}$ ) dominate early in Q2, and again in Q3 between the superoutbursts. The orbital signal ( $P_{\text{orb}} = 2.11$  hr,  $\nu_{\text{orb}} = 11.4$  c d $^{-1}$ ) is apparent during Q4, and once identified, during the week before the second superoutburst.

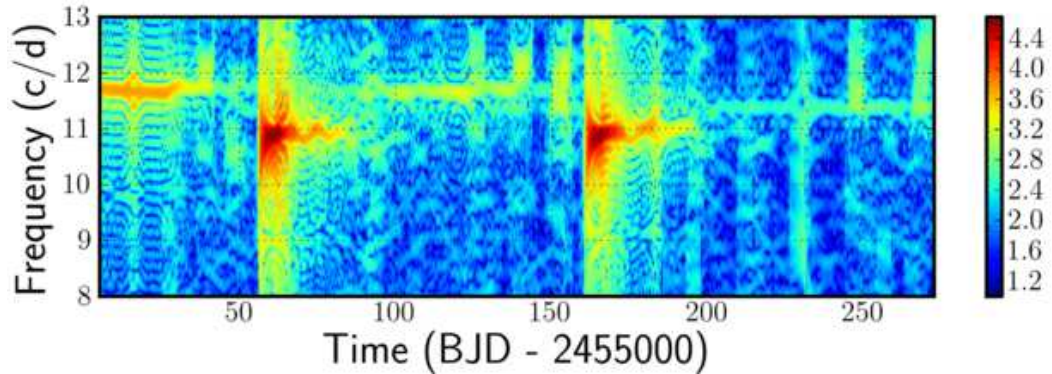


FIG. 11.— Magnified view of the 2D DFT for quarters Q2, Q3, and Q4. Shown here is the logarithm of the amplitude versus time and frequency. The three distinct frequencies are clearly evident. In days  $\sim 2$ –40 and again in days  $\sim 100$ –160, the  $P_- = 2.06$  hr period ( $\nu_- = 11.7$  c d $^{-1}$ ) indicative of the negative superhump dominates. The positive superhumps ( $P_+ = 2.20$  hr,  $\nu_+ = 10.9$  c d $^{-1}$ ) dominate the power for days  $\sim 58$ –80 and  $\sim 162$ –190. The orbital period ( $P_{\text{orb}} = 2.11$  hr,  $\nu_{\text{orb}} = 11.4$  c d $^{-1}$ ) is most clearly apparent in the Q4 data, starting about day 200.

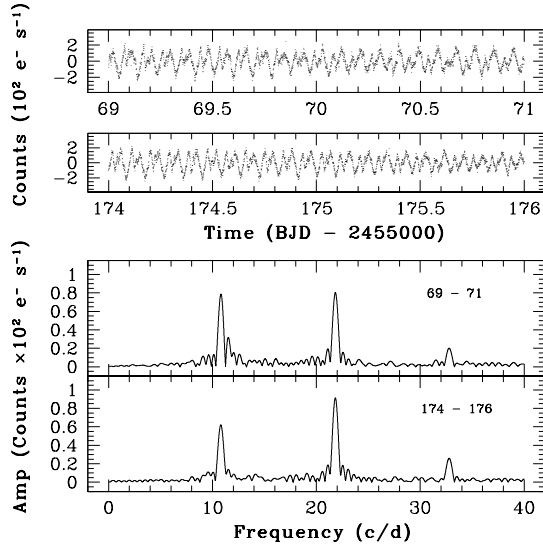


FIG. 12.— Light curves and associated Fourier transforms during the transition from disk to stream superhumps. As the system transitions from disk to stream superhumps in the drop to quiescence, the light curve is strongly double peaked but non-sinusoidal, resulting in power at both  $\nu_+$  and  $2\nu_+$  (first and second harmonics).

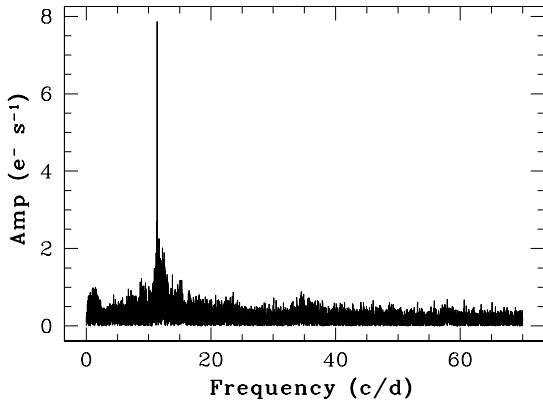


FIG. 13.— The Fourier transform obtained using the Q4 residual data. The single dominant peak is at 11.38 c/d (2.11 hr). We identify this as the orbital period.

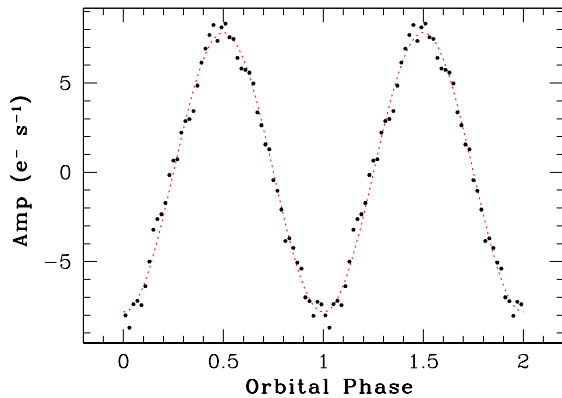


FIG. 14.— The average pulse peak shape for the identified orbital period, averaged over days 200-275 in Q4. Also shown for comparison is a sine curve.

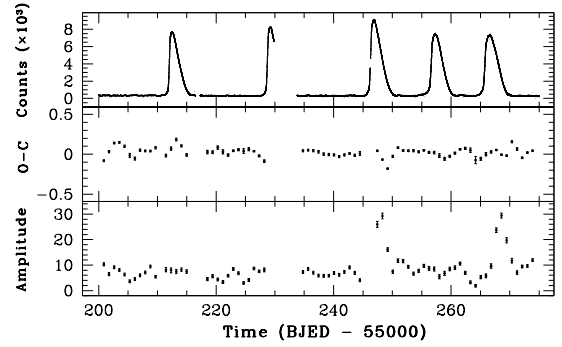


FIG. 15.— The O-C phase diagram for the identified orbital period  $P_{\text{orb}} = 2.10$  hr. For each point 20 cycles were fit, and each window is offset from the previous by 10 cycles. The bottom panel shows the amplitude of the fits to the residual light curves. The phase is steady, showing only small variations resulting from interference with other periods that are present, and that correlate with times of outburst. The large amplitudes found during outbursts 17 and 19 result from the higher-frequency signal initiated on decline from maximum in each case (see Figure 16).

cant digit are the *formal* errors from the fits summed in quadrature. The periods drift significantly during a superoutburst, however, indicating these formal error estimates should not be taken seriously. Using the periods found for the superhumps and orbit, we find a period excess of  $\epsilon_+ = 4.4\%$ . We plot the result for V344 Lyr with the results from the well-determined systems below the period gap listed in Table 9 of Patterson et al. (2005) in Figure 17. The period excess for V344 Lyr is consistent with the existing data.

In Figures 18 and 19 we show the time evolution of the mean pulse shape for the first and second superoutbursts. To create these Figures, we split the data into 5-day subsets ( $\sim 50$  cycles), with an overlap of roughly 2.5 days from one subset to the next. For each subset we computed a discrete Fourier transform and then folded the data on the period with the most power.

The evolution of the mean pulse shape is similar to results published previously (e.g. Patterson et al. 2003; Kato et al. 2009, 2010), however the quality of the *Kepler* data is such that we can test vigorously the model that has been slowly emerging in the past few years for the origin of the superhump light source, the evolution of the pulse shape and the physical origin of late superhumps.

A comparison of the simulation light curve from Figure 1 with the early mean pulse shapes shown in Figures 18 and 19 reveals a remarkable similarity, all the more remarkable given the very approximate nature of the artificial viscosity prescription used in the SPH calculations and the crude way in which the simulation light curves are calculated.

If the comparison between data and model is correct, the SPH simulations illuminate the evolution of the positive superhumps from the early disk-dominated source to the late stream-dominated source. The signal observed early in the superoutburst is dominated by disk superhumps, where the disk at resonance is driven into a large-amplitude oscillation, and viscous dissipation in the strongly convergent flows that occur once per superhump cycle yield the characteristic large-amplitude superhumps seen in the top panels of Figures 18 and 19. After  $\sim 100$  cycles ( $\sim 10$  d), a significant amount of mass has drained from the disk, and in particular from



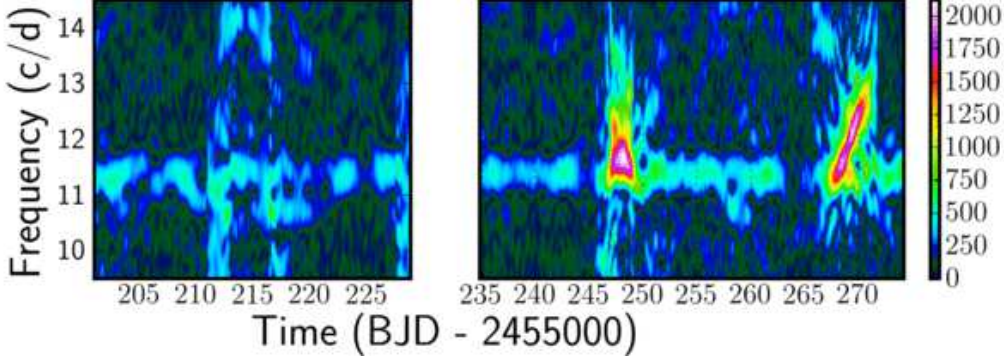


FIG. 16.— The 2D DFT of the post-superoutburst Q4 data. Shown are amplitude per cadence versus time and frequency. The window width was 2 days, and the window was shifted 1/8 day between transforms. The orbital signal is present but weak for most of the quarter. Power at a higher frequency is found on the decline from maximum in outbursts 17 and 19.

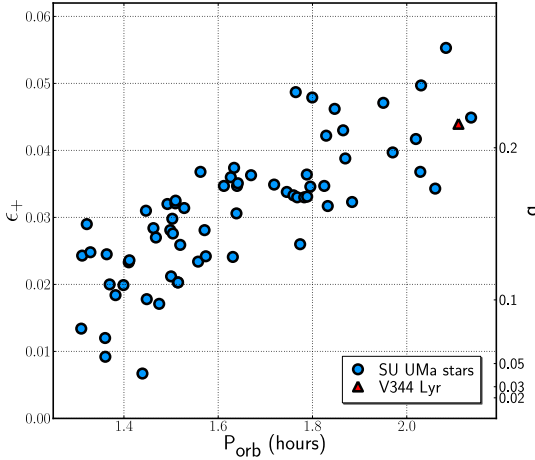


FIG. 17.— Measured period excess versus  $P_{\text{orb}}$  data from (Patterson et al. 2005) (circles) and for V344 Lyr (triangle). The system V344 Lyr is consistent with the trend.

the driving region. The disk continues to oscillate in response to the driving even after it has transitioned back to the quiescent state, but the driving is off-resonance and the periodic viscous dissipation described above is much reduced. Thus, we agree with previous authors that the late/quiescent superhumps that have been observed result from the dissipation in the bright spot as it sweeps around the rim of the non-axisymmetric disk.

To compute O-C phase diagrams for each superoutburst, we fit a 3-cycle sine curve with the mean period of 2.196 hr which yields a relatively constant O-C during the plateau phase. The results are shown in Figures 20 and 21. The top panel shows the residual light curve as well as the SAP light curve smoothed with a window width of  $P_+$  (135 points). The second panel shows the O-C phase diagram, and the third panel the amplitude of the fit. Also included in this Figure in the fourth panel are the periods of the positive superhumps during 2-day subsets of the residual light curve obtained with Fourier transforms. The horizontal bars show the extent of each data window. By differencing adjacent periods, we calculate the localized rate of period change of the superhumps  $\dot{P}_+$ . These results are shown in the bottom panel. As perhaps might be expected from the similarity in the evolution of the mean pulse profile during the two superoutbursts, the O-C phase diagrams as well as the evolution of the periods and localized rates of period

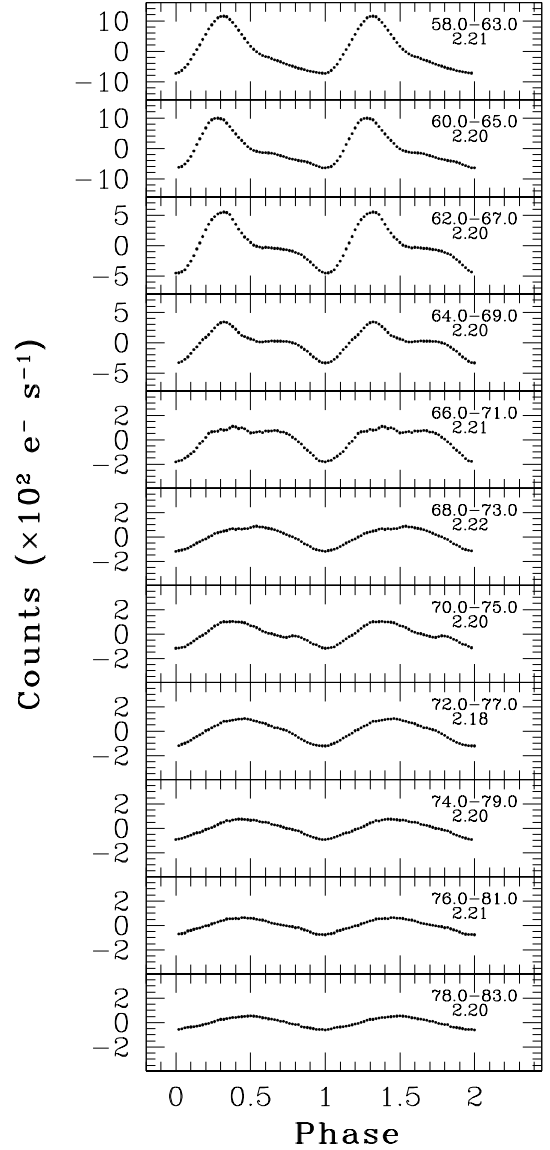


FIG. 18.— The average positive superhump pulse shapes obtained during the first superoutburst. The time spans of each 5-day subset of data and the folding periods (in hr) are indicated in each subpanel. Zero phase is set at the primary minimum. The mean pulse shape evolves considerably over the superoutburst. Note the changing vertical scale in the top-few panels.

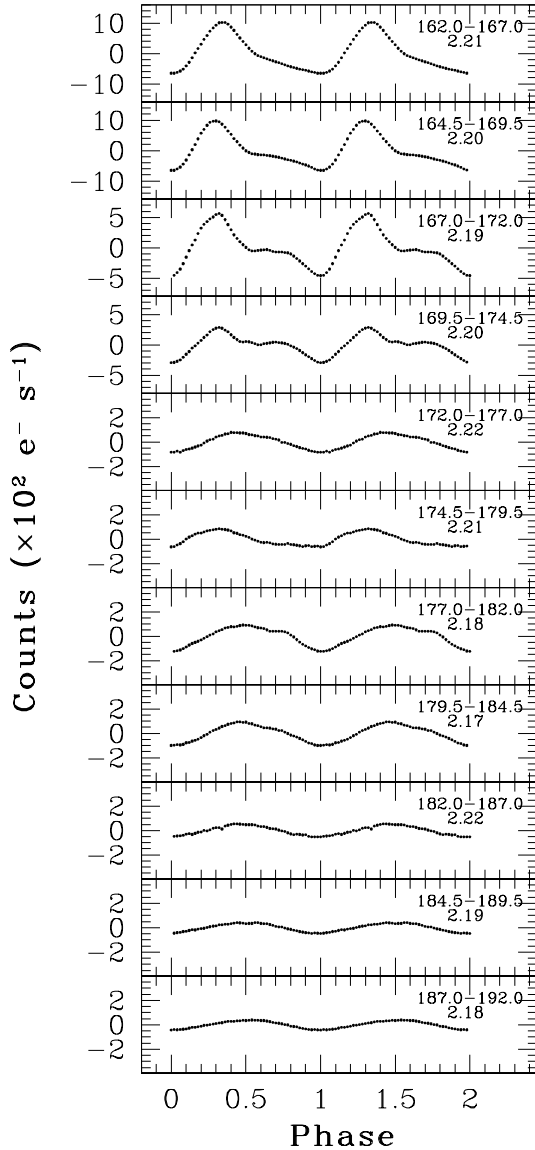


FIG. 19.— Similar to Figure 18, but for the second superoutburst. What is particularly interesting is that the evolution of the pulse shape is remarkably similar to that seen in the first superoutburst, suggesting that the dynamical evolution is also similar from one outburst to the next.

change are also similar. Such diagrams can be illuminating in the study of superhumps, and Kato et al. (2009) and Kato et al. (2010) present a comprehensive population analysis of superhumps using this method.

When the disk is first driven to oscillation in the growth and saturation phase, there is maximum mass at large radius, and the corresponding superhump period ( $\sim 2.25$  hr) is significantly longer than the mean, yielding a positive slope in the O-C diagram. The rate of period change estimated from the first 4 days of data for both superoutbursts is  $\dot{P}_+ = -8 \times 10^{-4} \text{ s s}^{-1}$ . Roughly 10 cycles ( $\sim 1$  d for V344 Lyr) after the mode saturates with maximum amplitude, sufficient mass has drained from the outer disk that the superhump period has decreased to the mean, and the superhump period continues to decrease out to  $E \sim 100$  as the precession rate slows as a result of the decreasing mean radius of the flexing, non-

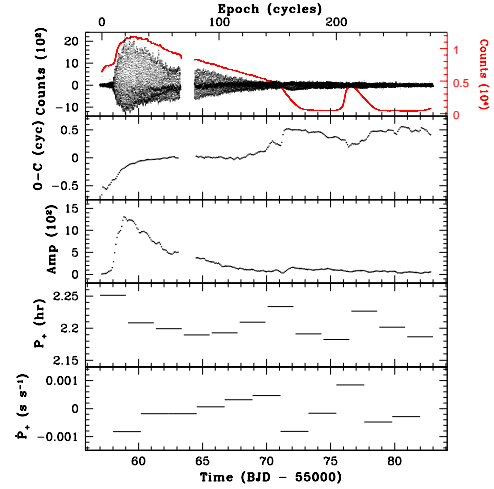


FIG. 20.— The residual light curve (black) in units of  $10^2 e^- s^{-1}$  and smoothed SAP light curve (red) in units of  $10^4 e^- s^{-1}$  (top panel), O-C phase diagram (second panel), amplitudes (third panel), period  $P_+$  (fourth panel) and localized rates of period change  $\dot{P}_+$  (bottom panel) for the common superhumps present during the first superoutburst. The observed phase variations reflect real variations in the oscillation period as well as the transition in the dominant modulation source for the light curve. The Epoch was arbitrarily set to zero for the first datum in this subset of the time series.

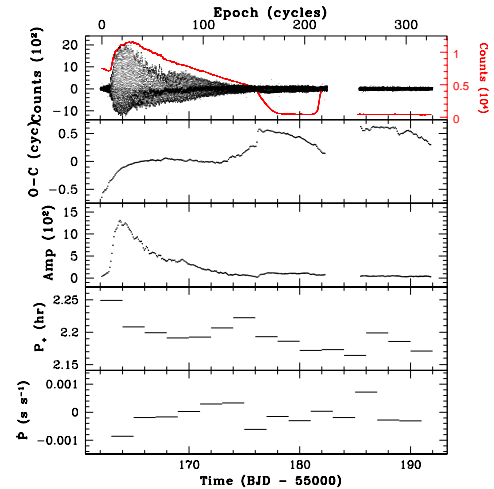


FIG. 21.— Similar to Figure 20, but for the second superoutburst. This Figure clearly shows that the phase variations have the same character as before, but with slightly larger excursions from the mean.

axisymmetric disk. The period at this time is roughly 2.19 hr for both superoutbursts, and the rate of period change between cycles 30 and 70 which includes the early plateau phase before the stream signal becomes important is  $\dot{P}_+ = -1.8 \times 10^{-4} \text{ s s}^{-1}$ .

Between cycles  $\sim 110$  and 150, the O-C phase diagrams in Figures 20 and 21 show phase shifts of  $\sim 0.5$  cycles. This is the result of the continued fading of the disk superhump, and the transition to the stream/late superhump signal. Careful inspection of the top panels of Figures 20 and 21 near days 68 and 174 in fact shows the decreasing amplitude of the disk superhump, and the relatively constant amplitude of the stream superhump. By cycle  $\sim 150$  (days  $\sim 72$  and 176), the disk superhump



amplitude is negligible, and all that remains is the signal from the stream superhump. The smoothed SAP light curve shown in the top panel shows that these times correspond to the return to the quiescent state during which the global viscosity is again low. It is also interesting that  $\dot{P}_+$  itself appears to be increasing relatively linearly during much of the plateau phase with an average rate of  $\dot{P}_+ \sim 10^{-9} \text{ s}^{-1}$ . At present this is not explained by the numerical simulations. It may simply be that this result reflects the growing relative importance of the stream superhump signal on the phase of the 3-cycle sine fit. This is almost certainly the case during the period peaks found at days  $\sim 71$  and  $175$ , where we find that the sine fits are pulled to longer period by the complex and rapidly changing waveform (e.g., Figure 12).

In the quiescent interval before the first subsequent outburst the O-C diagram shows a concave-downward shape indicating a negative  $\dot{P}_+ \sim -2 \times 10^{-4} \text{ s s}^{-1}$ . We speculate that the behavior of the O-C curve in response to the outburst following the first superoutburst may indicate that the outburst may effectively expand the radius of the disk causing a faster apsidal precession. Unfortunately, there is a gap in the *Kepler* data that starts just after the initial rise of the outburst following the second superoutburst. The value of  $\dot{P}_+$  averaged over the the last 2 measured bins for both superoutbursts is  $\dot{P}_+ \sim -3 \times 10^{-4} \text{ s s}^{-1}$ .

The measured values of  $\dot{P}_+$  for V344 Lyr are consistent with those reported in the extensive compilation of Kato et al. (2009). To make a direct comparison with Kato et al., who calculate  $\dot{P}_+$  over the first 200 cycles (i.e., plateau phase), we average all the  $\dot{P}_+$  measurements out to the drop to quiescence, and find an average value of  $-6 \times 10^{-5} \text{ s s}^{-1}$  for the first superoutburst and  $-9 \times 10^{-5} \text{ s s}^{-1}$  for the second. These values for V344 Lyr are entirely consistent with the Kato et al. results as shown in their Figure 8.

In Still et al. (2010) we noted that V344 Lyr was unusual (but not unique) in that superhumps persist into quiescence and through the following outburst in Q2. Other systems that have been observed to show (late) superhumps into quiescence more typically have short orbital periods, including V1159 Ori (Patterson et al. 1995), ER UMa (Gao et al. 1999; Zhao et al. 2006), WZ Sge (Patterson et al. 2002b), and the WZ Sge-like star V466 And (Chochol et al. 2010), among others. The identification of late superhumps is a matter of contention in some cases (Kato et al. 2009), and the post-superoutburst coverage of targets is more sparse than the coverage during superoutbursts. Thus it is difficult to know if post-superoutburst superhumps are common or rare at this time.

#### 4.3. Observed Negative Superhumps

As noted above in §2.2, the 2.06-hr (11.4 c/d) signal that dominates the light curve for the first  $\sim 35$  days of Q2 is now understood to be the result of a negative superhump. This yields a value for the period deficit (Equation 3) of  $\epsilon_- = 2.5\%$ . The maximum amplitude at quiescence is  $A \sim 0.8$  mag. Figure 22 shows 10 cycles of the negative superhump signal during this time. The inset shows the mean pulse shape averaged over days 5 to 25

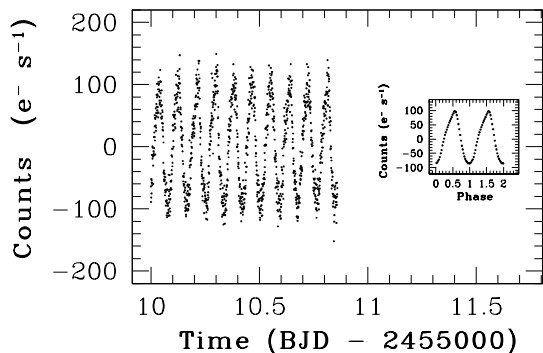


FIG. 22.— The Figure shows 10 cycles of the negative superhump signal. The inset shows the average pulse shape over days 5 to 25. The signal is sawtoothed with a rise time roughly twice the fall time, and appears consistent with the ray-traced SPH simulation pulse shapes published by Wood & Burke (2007).

(roughly 230 cycles). The signal is approximately sawtoothed with a rise time roughly twice the fall time. It appears consistent with the pulse shapes Wood & Burke (2007) obtained using ray-trace techniques on 3D simulations of tilted disks (their Figure 3). Negative superhumps dominate the power in days  $\sim 2$ –35 and again in days  $\sim 100$ –160.

The signal observed near the beginning of Q2 reveals a remarkably large rate of period change – large enough that it can be seen in the harmonics of the Fourier transform shown in Figure 10 as a negative slope towards lower frequency with time. A nonlinear least squares fit to the fundamental period measured during days 2.5–7.5 yields  $P_- = 2.05006 \pm 0.00005$  hr. A fit to the data from days 22–26, however, yields  $P_- = 2.06273 \pm 0.00005$  hr. The formal errors from non-linear least squares fits underestimate the true errors by as much an order of magnitude (Montgomery & Odonoghue 1999), but even if this is the case, these two results differ by  $\sim 25\sigma$ . Taken at face value, they yield a rate of period change of  $\dot{P}_- \sim 3 \times 10^{-5} \text{ s s}^{-1}$ . Similarly, we fit the negative superhump periods in two 4-day windows centered on days 112.0 and 121.0. The periods obtained from non-linear least squares are  $P_- = 2.0530 \pm 0.0002$  hr and  $P_- = 2.066038 \pm 0.00008$  hr, respectively, which yields  $\dot{P}_- \sim 6 \times 10^{-5} \text{ s s}^{-1}$  over this time span. In their recent comprehensive analysis of the evolution of CVs as revealed by their donor stars, Knigge et al. (2011) estimate that for systems with  $P_{\text{orb}} \sim 2$  hr the rate of orbital period change should be  $\dot{P}_{\text{orb}} \sim -7 \times 10^{14} \text{ s s}^{-1}$  (see their Figure 11). Clearly the  $\sim 2.06$ -hr signal cannot be orbital in origin. In some negatively superhumping systems with high inclinations, the precessing tilted disk can modulate the mean brightness (e.g. Stanishev et al. 2002). We found no significant signal in the Fourier transform at the precession period of  $\sim 3.6$  d.

In Figure 23 we show the results of the O-C analysis for the Q2 data. To create the Figure, we fit 5-cycle sine curves of period 2.05 hr to the residual light curve, shifting the data by one cycle between fits. The shape of the O-C diagram is concave up until the peak of the first outburst at day  $\sim 28$  indicating that the period of the signal is lengthening during this time span. The magnitude of the negative superhump period deficit is inversely related to the retrograde precession period of the tilted disk – a

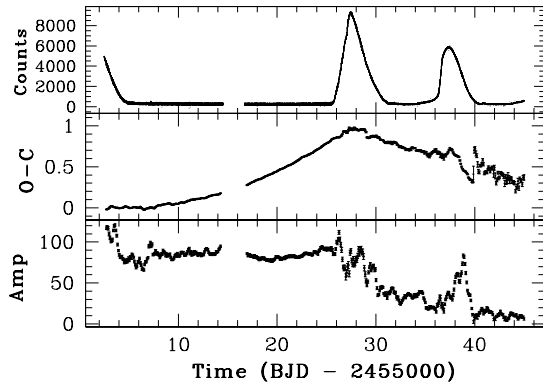


FIG. 23.— The SAP light curve (top panel) O-C phase diagram (middle panel) and amplitude (bottom panel) of the negative superhump signal during days 2.5 to 45.0. A 5-cycle sinusoid was fit to the data, moving the window 1 cycle between fits. The amplitude of the signal is large and relatively constant initially, and the phase variations are concave upward, indicating a lengthening period. During outburst 1, there is a cusp in the O-C diagram, indicating a jump to shorter period, and after outburst 1, the amplitude begins to decline.

shorter precession period yields a larger period deficit. A disk that was not precessing at all would show a negative superhump period equal to the orbital period. The observation that the negative superhump period in V344 Lyr is lengthening during days  $\sim 2$  to 27 indicates that the precession period of the tilted disk is increasing (i.e., the rate of precession is decreasing). Coincident with the first DN outburst (outburst 1) in Q2, there is a cusp in the O-C diagram, indicating a jump to shorter period (faster retrograde precession rate). The amplitude of the signal begins to decline significantly following outburst 1, and the signal is effectively quenched by outburst 2. Note that between days  $\sim 28$  and 35 the O-C diagram is again concave up, although with less curvature than before outburst 1.

We show the 2D DFT of the pre-superoutburst Q2 data in Figure 24. Here we used a window width of 2 days that was shifted  $1/8$  day between transforms. We plot the amplitude in counts per cadence. It is evident that outburst 1 shifts the oscillation frequency, as well quenching the amplitude of the signal. Outburst 2 triggers a short-lived signal with a period of roughly  $11.9$  c/d ( $2.02$  hr), and outburst 3 appears to generate signals near the frequencies of the negative and positive superhumps that rapidly evolve to higher and lower frequencies, respectively, only to fade to noise background by the end of the outburst. Outburst 3 has a somewhat slower rise to maximum than most of the outbursts in the time series and is the last outburst before the first superoutburst, but is otherwise unremarkable. This is the only time we see this behavior in the 3 quarters of data we present, so it is unclear what the underlying physical mechanism is.

Although much of the Q3 light curve is dominated by the negative superhump signal, the amplitude is much lower than early in Q2, and in addition there is contamination from the orbital and positive superhump signals. In Figure 25 we show the 2D DFT for the Q3 data between days 93 and 162, again showing the amplitude in counts per cadence versus time and frequency. We used a window width of 2 days that was shifted  $1/8$  day between transforms.

In Figure 26 we show the O-C phase diagram obtained

by fitting a 5-cycle sine curve of period 2.06 hr to data spanning days 93.2 to 140.0. The amplitude during this time is considerably smaller than was the case for the Q2 negative superhumps. Before day 106, there appears to be contamination from periodicities near the superhump frequency of  $10.9$  c/d that are evident in Figure 25, and after day 126 the signal fades dramatically. It was only during days 106.5 to 123.2 that the amplitude of the negative superhump signal was large enough, stable enough, and uncontaminated to yield a clean O-C phase diagram. These data lie between outbursts 8 and 9, and comprise the longest quiescent stretch in Q3. It can be seen that the O-C curve is again concave upward indicating a positive rate of period change as calculated above, and the bottom panel indicates that the amplitude of the signal is increasing during this time span.

The retrograde precession rate of a tilted accretion disk is a direct function of the effective (mass weighted) radius of the disk. Several groups have studied the precession properties of tilted disks (Papaloizou & Terquem 1995; Larwood et al. 1996; Larwood 1998; Larwood & Papaloizou 1997; Lai 1999). Papaloizou et al. (1997) derived the following expression for the induced precession frequency  $\omega_p$  of a tilted accretion disk,

$$\omega_p = -\frac{3}{4} \frac{GM_2}{a^3} \frac{\int \Sigma r^3 dr}{\int \Sigma \Omega r^3 dr} \cos \delta \quad (5)$$

where  $\omega_p$  is the leading-order term of the induced precession frequency for a differentially rotating fluid disk, calculated using linear perturbation theory,  $\Sigma(r)$  is the axisymmetric surface density profile and  $\Omega(r)$  the unperturbed Keplerian angular velocity profile,  $a$  is the orbital separation,  $M_2$  is the mass of the secondary, and  $\delta$  is the tilt of the disk with respect to the orbital plane. The integrals are to be taken between the inner and outer radii of the disk.

In a later study of the precession of tilted accretion disks, Larwood (1997, and see Larwood (1998)) derived the expression for the precession frequency of a disk with constant surface density  $\Sigma$  and polytropic equation of state with ratio of specific heats equal to  $5/3$ :

$$\frac{\omega_p}{\Omega_0} = -\frac{3}{7} q \left( \frac{R_0}{a} \right)^3 \cos \delta, \quad (6)$$

where here  $\Omega_0$  is the Keplerian angular velocity of the outer disk of radius  $R_0$ , and  $q$  is the mass ratio.

The physical interpretation of Equations 5 and 6 is that tilted accretion disks weighted to larger radii will have higher precession frequencies than those weighted to smaller radii. For example, if we have 2 disks with the same nominal tilt and total mass, where one has a constant surface density and the other with a surface density that increases with radius, the second disk will have a higher precession rate, and would yield a negative superhump frequency higher than the first. A third disk with most of its mass concentrated at small radius would have a lower precession frequency and yield a negative superhump signal nearest the orbital signal.

In this picture the increasing precession period indicated by the positive rate of period change for the negative superhump signal  $\dot{P}_-$  might at first seem counter-

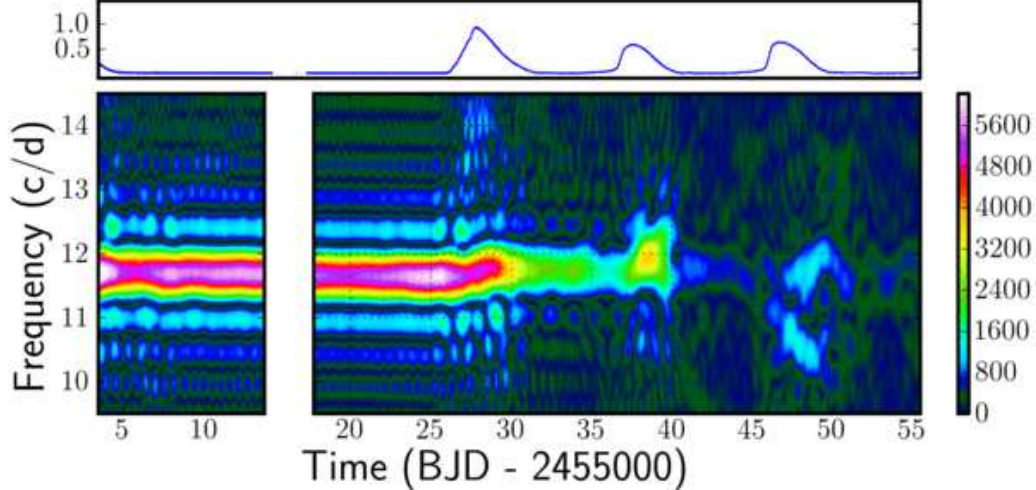


FIG. 24.— The 2D DFT of the pre-superoutburst Q2 data. Shown are amplitude per cadence versus time and frequency. The window width was 2 days, and the window was shifted 1/8 day between transforms. Most obvious is that the first outburst shifts the power to higher frequency, but careful inspection also shows that the frequency evolves towards longer period up to day  $\sim 25$  (e.g., note the slope of the sidelobe at  $\sim 11$  c/d with respect to the grid line). Outbursts 2 and 3 both appear to generate power on the decline from maximum.

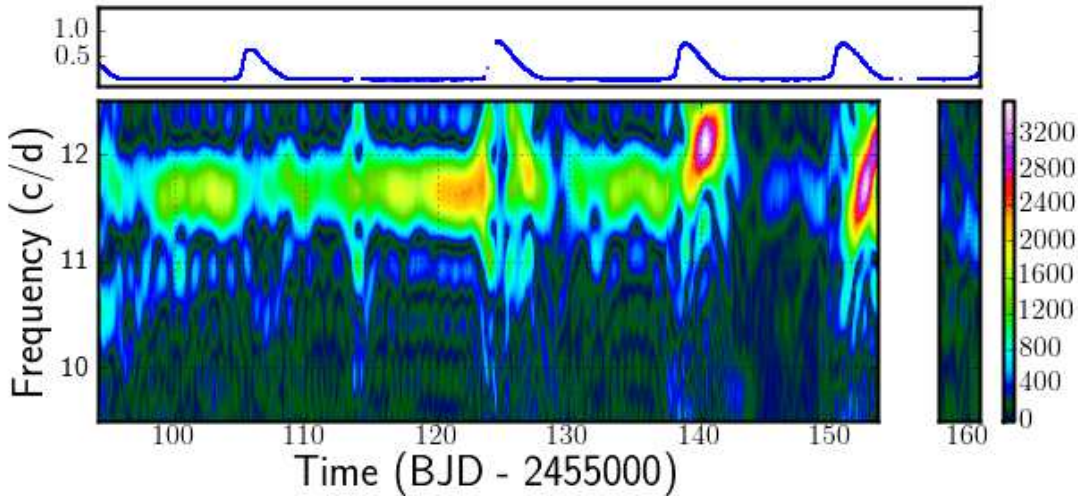


FIG. 25.— The 2D DFT of the inter-superoutburst Q3 data. Shown are amplitude per cadence versus time and frequency. The window width was 2 days, and the window was shifted 1/8 day between transforms. The negative superhump signal is present until day  $\sim 140$ . Higher-frequency power is generated on the decline from maximum of the last 2 outbursts.

intuitive since the disk is gaining mass at quiescence. However, the key fact is that tilted disks accrete most of their mass at *small* radii, since the accretion stream impacts the face of the tilted disk along the line of nodes (Wood & Burke 2007; Wood et al. 2009). The accretion stream impacts the rim of the disk only twice per orbit (refer back to Figure 5). Thus, the effective (mass weighted) radius of an accreting tilted disk *decreases* with time, causing a slowing in the retrograde precession rate  $\omega_p$ , and an increase in the period of the negative superhump signal  $P_-$ .

A detailed analysis of the data, theory, and numerical model results should allow us to probe the time evolution of the mass distribution in disks undergoing negative superhumps, and hence the low-state viscosity mechanism. The unprecedented quality and quantity of the *Kepler* time series data suggests that V344 Lyr and perhaps other *Kepler*-field CVs that display negative superhumps may significantly advance our understanding of the evo-

lution of the mass distribution in tilted accretion disks.

The cause of disk tilts in CVs is still not satisfactorily explained. In the low-mass x-ray binaries it is believed that radiation pressure can provide the force necessary to tilt the disk out of the orbital plane (Petterson 1977; Iping & Petterson 1990; Foulkes et al. 2006; Ivanov & Papaloizou 2008), however this mechanism is not effective in the CV scenario. Barrett et al. (1988) suggested in their work on TV Col that magnetic fields near the L1 region might deflect the accretion stream out of the orbital plane, but as noted in Wood & Burke (2007) the orbit-averaged angular momentum vector of a deflected stream would still be parallel to the orbital angular momentum variable. Murray et al. (2002) demonstrated numerically that a disk tilt could be generated by instantaneously turning on a magnetic field on the secondary star. Although their tilt decayed with time (the orbit-averaged angular momentum argument again), their results suggest that

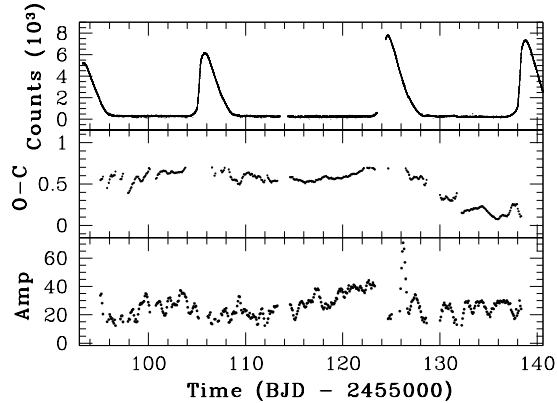


FIG. 26.— The SAP light curve (top panel) O-C phase diagram (middle panel) and amplitude (bottom panel) of the negative superhump signal during days 106.5 to 123.2. As in Figure 23, the shape of the O-C curve is concave upward, indicating a positive rate of period change.

changing magnetic field geometries could generate disk tilt. Assuming that the disk viscosity is controlled by the MRI (Balbus & Hawley 1998; Balbus 2003), it is plausible that differentially-rotating plasmas may also be subject to magnetic reconnection events (flares) which are asymmetrical with respect to the disk plane, or that during an outburst the intensified disk field may couple to the tilted dipole field on the primary star (e.g., Lai 1999) or the field of the secondary star (Murray et al. 2002).

With these ideas in mind, the behavior of V344 Lyr during outbursts 2, 10, 11, 17, and 19 is tantalizing. First, again consider the 2D DFTs from Q2, Q3, and Q4 shown in Figures 24, 25 and 16, respectively. In each of these cases, there is power generated at a frequency consistent with the negative superhump frequency on the decline from maximum light. Outbursts 2 and 10 appear to excite a frequency of roughly 12 c/d ( $\sim 2$  hr), outburst 17 excites the negative superhump frequency for  $\sim 3$  days, and outbursts 11 and 19 appear to excite power at the negative superhump frequency that rapidly evolves to shorter frequencies. We show the SAP light curves for these outbursts as well as the residual light curves in Figure 27. The residual light curves for these 5 outbursts all appear to show the excitation of a frequency near or slightly greater than the negative superhump frequency that dominates early in Q2. This is about  $1/3$  of the normal outbursts in the 3 quarters of *Kepler* data – the other 12 outbursts do not show evidence for having excited new frequencies. Thus, while additional data are clearly required and our conclusions are speculative, we suggest that these results support a model in which the disk tilt is generated by the transitory (impulsive) coupling between an intensified disk magnetic field and the field of the primary or secondary star. The fact that these 5 outburst events yield frequencies near 12 c/d appears to support the model that it is the mass in the outer disk that is initially tilted out of the plane.

## 5. CONCLUSIONS

We present the results of the analysis of 3 quarters of *Kepler* time series photometric data from the system V344 Lyr. Our major findings are:

1. The orbital, negative superhump, and positive superhump periods are  $P_{\text{orb}} = 2.11$  hr,  $P_- = 2.06$

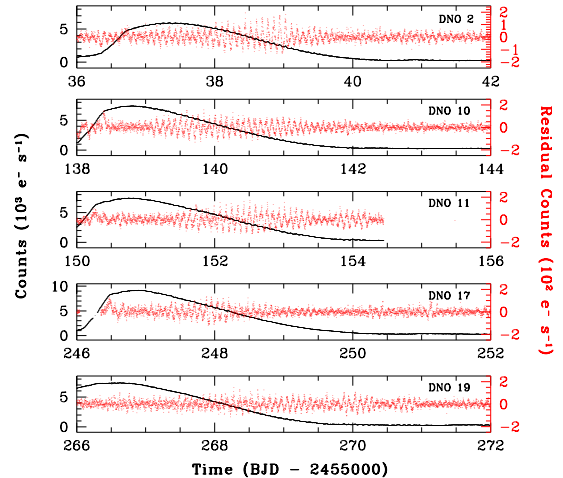


FIG. 27.— Dwarf nova outbursts 2, 10, 11, 17, and 19, each showing oscillations on the decline from maximum. The black points show the SAP light curves, summed two points for clarity. The red points show the residual light curves, also summed two points.

hr, and  $P_+ = 2.20$  hr, giving a positive superhump period excess of  $\epsilon_+ = 4.4\%$ , and a negative superhump period deficit of  $\epsilon_- = 2.5\%$ .

2. The quality of the *Kepler* data is such that we can constrain significantly the models for accretion disk dynamics that have been proposed in the past several years.
3. The evolution of the pulse shapes and phases of the positive superhump residual light curve provides convincing evidence in support of the two-source model for positive superhumps. Early in the superoutburst, viscous dissipation in the strongly convergent flows of the flexing disk provide the modulation observed at the superhump frequency. Once the system has returned to quiescence, the modulation is caused by the periodically-variable dissipation at the bright spot as it sweeps around the rim of the still non-axisymmetric, flexing disk. During the transition the O-C phase diagram shows a shift of  $\sim 0.5$  in phase.
4. Superoutbursts begin as normal DN outbursts. The rise to superoutburst is largely explained by the thermal-viscous limit cycle model discussed in Paper II. Beyond this luminosity source which does a reasonable job of matching the lower envelope of the superoutburst light curve, there is additional periodic dissipation that generates the superhump signals. The sources of the periodic dissipation are (i) the strongly convergent flows that are generated once per superhump cycle as the disk is compressed in the radial direction opposite the secondary, and (ii) the variable depth of the bright spot as it sweeps around the rim of the non-axisymmetric oscillating disk.
5. Numerical experiments that individually isolate the two proposed physical sources of the positive superhump signal yield results that are broadly consistent with the signals in the data.

6. The positive superhumps show significant changes in period that occur in both superoutbursts. The average  $\dot{P}_+ \sim 6 \times 10^{-5} \text{ s s}^{-1}$  for the first superoutburst and  $\dot{P}_+ \sim 9 \times 10^{-5} \text{ s s}^{-1}$  for the second are consistent with literature results. The data reveal that  $\dot{P}_+$  itself appears to be increasing relatively linearly during much of the plateau phase at an average rate for the two superoutbursts of  $\ddot{P} \sim 10^{-9} \text{ s}^{-1}$ .
7. The negative superhumps show significant changes in period with time, resulting from the changing mass distribution (moment of inertia) of the tilted disk. As the mass of the inner disk increases before outburst 1, the retrograde precession period increases, consistent with theoretical predictions. These data are rich with unmined information.
8. Negative superhumps appear to be excited as a direct result of some of the dwarf nova outbursts. We speculate that the MRI-intensified disk field can couple to the field of the primary or secondary star and provide an impulse that tilts the disk out of the orbital plane. Continued monitoring by *Kepler* promises to shed light on this important unsolved problem.

The system V344 Lyr continues to be monitored at short cadence by the *Kepler* mission. It will undoubtedly become the touchstone system against which obser-

vations of all other SU UMa CVs will be compared, as the quantity and quality of the time series data are unprecedented in the history of the study of cataclysmic variables. The *Kepler* data for V344 Lyr promise to reveal details of the micro- and macrophysics of stellar accretion disks that would be impossible to obtain from ground-based observations.

*Kepler* was selected as the 10th mission of the Discovery Program. Funding for this mission is provided by NASA, Science Mission Directorate. All of the data presented in this paper were obtained from the Multi-mission Archive at the Space Telescope Science Institute (MAST). STScI is operated by the Association of Universities for Research in Astronomy, Inc., under NASA contract NAS5-26555. Support for MAST for non-HST data is provided by the NASA Office of Space Science via grant NAG5-7584 and by other grants and contracts. This research was supported in part by the American Astronomical Society's Small Research Grant Program in the form of page charges. We thank Marcus Hohlmann from the Florida Institute of Technology and the Domestic Nuclear Detection Office in the Dept. of Homeland Security for making computing resources on a Linux cluster available for this work. We thank Joseph Patterson of Columbia University for sending us the data used in Figure 19 in electronic form.

*Facilities: Kepler*

#### REFERENCES

- Ak, T., Bilir, S., Ak, S., & Eker, Z. 2008, *New Astronomy*, 13, 133  
 Balbus, S. A. 2003, *ARA&A*, 41, 555  
 Balbus, S. A., & Hawley, J. F. 1998, *Reviews of Modern Physics*, 70, 1  
 Barrett, P., O'Donoghue, D., & Warner, B. 1988, *MNRAS*, 233, 759  
 Bildsten L., Townsley D. M., Deloye C. J., Nelemans G., 2006, *ApJ*, 640, 466  
 Bonnet-Bidaud, J. M., Motch, C., & Mouchet, M. 1985, *A&A*, 143, 313  
 Borucki, W. J., et al. 2010, *Science*, 327, 977  
 Caldwell, D. A., et al. 2010, *ApJ*, 713, L92  
 Cannizzo, J. K. 1993, *Accretion Disks in Compact Stellar Systems*, ed. J. C. Wheeler (Singapore: World Scientific), 6  
 Cannizzo, J. K. 1993, *ApJ*, 419, 318  
 Cannizzo, J. K. 1998, *ApJ*, 494, 366  
 Cannizzo, J. K., Still, M. D., Howell, S. B., Wood, M. A., & Smale, A. P. 2010, *ApJ*, 725, 1393  
 Cannizzo, J. K., Smale, A. P., Still, M. D., Wood, M. A., & Howell, S. B. 2011, *ApJ*, submitted  
 Charles, P. A., Kidger, M. R., Pavlenko, E. P., Prokof'eva, V. V., & Callanan, P. J. 1991, *MNRAS*, 249, 567  
 Chochol, D., Katysheva, N. A., Shugarov, S. Y., Volkov, I. M., & Andreev, M. V. 2010, *Contributions of the Astronomical Observatory Skalnaté Pleso*, 40, 19  
 Faulkner, J., Flannery, B. P., & Warner, B. 1972, *ApJ*, 175, L79  
 Feldmeier, J. J., et al. 2011, *ApJ*, in press (arXiv:1103.3660)  
 Fontaine, G., et al. 2011, *ApJ*, 726, 92  
 Foulkes, S. B., Haswell, C. A., & Murray, J. R. 2006, *MNRAS*, 366, 1399  
 Frank, J., King, A., & Raine, D. J. 2002, *Accretion Power in Astrophysics*, by Juhan Frank and Andrew King and Derek Raine, pp. 398. ISBN 0521620538. Cambridge, UK: Cambridge University Press, February 2002.,  
 Gao, W., Li, Z., Wu, X., Zhang, Z., & Li, Y. 1999, *ApJ*, 527, L55  
 Gilliland, R. L., et al. 2010, *PASP*, 122, 131  
 Haas, M. R., et al. 2010, *ApJL*, 713, L115  
 Harvey, D. A., Skillman, D. R., Kemp, J., Patterson, J., Vanmunster, T., Fried, R. E., & Retter, A. 1998, *ApJ*, 493, L105  
 Hellier, C. 2001, *Cataclysmic Variable Stars: How and Why They Vary*, Springer-Praxis Books in Astronomy & Space Sciences: Praxis Publishing  
 Hessman, F. V., Mantel, K.-H., Barwig, H., & Schoembs, R. 1992, *A&A*, 263, 147  
 Howell, S. B., Reyes, A. L., Ashley, R., Harrop-Allin, M. K., & Warner, B. 1996, *MNRAS*, 282, 623  
 Hynes, R. I., et al. 2006, *ApJ*, 651, 401  
 Iping R. C., Petterson J. A., 1990, *A&A*, 239, 221  
 Ivanov P. B., Papaloizou J. C. B., 2008, *MNRAS*, 384, 123  
 Jenkins, J. M., et al. 2010, *ApJ*, 713, L87  
 Kato, T. 1993, *PASJ*, 45, L67  
 Kato, T., Poyner, G., & Kinnunen, T. 2002, *MNRAS*, 330, 53  
 Kato, T., et al. 2009, *PASJ*, 61, 395  
 Kato, T., et al. 2010, *PASJ*, 62, 1525  
 Kim, Y., Andronov, I. L., Cha, S. M., Chinarova, L. L., & Yoon, J. N. 2009, *A&A*, 496, 765  
 Knigge, C., Baraffe, I., & Patterson, J. 2011, *ApJS*, 194, 28  
 Koch, D. G., et al. 2010, *ApJ*, 713, L79  
 Kunze, S. 2002, in *ASP Conf. Series 261: The Physics of Cataclysmic Variables and Related Objects*, eds. B.T. Gänsicke, K. Beuermann, & K. Reinsch, 497  
 Kunze, S. 2004, *Revista Mexicana de Astronomia y Astrofisica Conference Series*, 20, 130  
 Lai, D. 1999, *ApJ*, 524, 1030  
 Larwood, J. D. 1997, *MNRAS*, 290, 490  
 Larwood, J. 1998, *MNRAS*, 299, L32  
 Larwood, J. D., Nelson, R. P., Papaloizou, J. C. B., & Terquem, C. 1996, *MNRAS*, 282, 597  
 Larwood, J. D., & Papaloizou, J. C. B. 1997, *MNRAS*, 285, 288  
 Lasota, J.-P. 2001, *New Astron. Rev.*, 45, 449  
 Mineshige, S., Hirose, M., & Osaki, Y. 1992, *PASJ*, 44, L15  
 Montgomery, M. H., & Odonoghue, D. 1999, *Delta Scuti Star Newsletter*, 13, 28

- Murray J. R., Chakrabarty D., Wynn G. A., Kramer L., 2002, *MNRAS*, 335, 247
- Nelemans, G. 2005, in ASP Conf. Ser. 330, *The Astrophysics of Cataclysmic Variables and Related Objects*, ed. J.-M. Hameury & J.-P. Lasota (San Francisco: ASP), 27
- Nelemans, G., Steeghs, D., & Groot, P. J. 2001, *MNRAS*, 326, 621
- O'Donoghue, D., & Charles, P. A. 1996, *MNRAS*, 282, 191
- Osaki, Y. 1985, *A&A*, 144, 369
- Osaki, Y. 1989, *PASJ*, 41, 1005
- Papaloizou, J. C. B., Larwood, J. D., Nelson, R. P., & Terquem, C. 1997, *Accretion Disks - New Aspects*, 487, 182
- Papaloizou, J. C. B., & Terquem, C. 1995, *MNRAS*, 274, 987
- Patterson, J. 1999, in *Disk Instabilities in Close Binary Systems*, eds. S. Mineshige and J. C. Wheeler, (Kyoto: Universal Acad. Press), 61
- Patterson, J., Halpern, J., & Sharnbrook, A. 1993, *ApJ*, 419, 803
- Patterson, J., Jablonski, F., Koen, C., O'Donoghue, D., & Skillman, D. R. 1995, *PASP*, 107, 1183
- Patterson, J., Kemp, J., Jensen, L., Vanmunster, T., Skillman, D. R., Martin, B., Fried, R., & Thorstensen, J. R. 2000, *PASP*, 112, 1567
- Patterson, J., Sterner, E., Halpern, J. P., & Raymond, J. C. 1992, *ApJ*, 384, 234
- Patterson, J., Thomas, G., Skillman, D. R., & Diaz, M. 1993, *ApJS*, 86, 235
- Patterson, J., et al. 2002, *PASP*, 114, 65
- Patterson, J., et al. 2002, *PASP*, 114, 721
- Patterson, J., et al. 2003, *PASP*, 115, 1308
- Patterson, J., et al. 2005, *PASP*, 117, 1204
- Patterson J. A., 1977, *ApJ*, 216, 827
- Provencal, J. L., et al. 1995, *ApJ*, 445, 927
- Retter, A., Leibowitz, E. M., & Ofek, E. O. 1997, *MNRAS*, 286, 745
- Retter, A., Chou, Y., Bedding, T. R., & Naylor, T. 2002, *MNRAS*, 330, L37
- Roelofs, G. H. A., Groot, P. J., Nelemans, G., Marsh, T. R., & Steeghs, D. 2007, *MNRAS*, 379, 176
- Rolfe, D. J., Haswell, C. A., & Patterson, J. 2001, *MNRAS*, 324, 529
- Schoembs, R. 1986, *A&A*, 158, 233
- Simpson, J. C., & Wood, M. A. 1998, *ApJ*, 506, 360
- Skillman, D. R., Harvey, D., Patterson, J., & Vanmunster, T. 1997, *PASP*, 109, 114
- Skillman, D. R., Patterson, J., Kemp, J., Harvey, D. A., Fried, R. E., Retter, A., Lipkin, Y., & Vanmunster, T. 1999, *PASP*, 111, 1281
- Smak, J. 1967, *Acta Astron.*, 17, 255
- Smak, J. 2007, *Acta Astron.*, 57, 87
- Smak, J. 2008, *Acta Astron.*, 58, 55
- Smak, J. 2009, *Acta Astron.*, 59, 121
- Smak, J. 2010, *Acta Astron.*, 60, 357
- Smak, J. 2011, *Acta Astron.*, 61, 59
- Smith, A. J., Haswell, C. A., Murray, J. R., Truss, M. R., & Foulkes, S. B. 2007, *MNRAS*, 378, 785
- Solheim, J.-E. 2010, *PASP*, 122, 1133
- Stanishev, V., Kraicheva, Z., Boffin, H. M. J., & Genkov, V. 2002, *A&A*, 394, 625
- Sterken, C., Vogt, N., Schreiber, M. R., Uemura, M., & Tuvikene, T. 2007, *A&A*, 463, 1053
- Still, M., Howell, S. B., Wood, M. A., Cannizzo, J. K., & Smale, A. P. 2010, *ApJ*, 717, L113
- Templeton, M. R., et al. 2006, *PASP*, 118, 236
- Van Cleve, J., ed. 2010, *Kepler Data Release Notes 6*, KSCI-019046-001.
- Vogt, N. 1982, *ApJ*, 252, 653
- Warner, B. 1995a, *Cataclysmic Variable Stars* (Cambridge: Cambridge University Press)
- Warner, B. 1995b, *Ap&SS*, 225, 249
- Whitehurst, R. 1988, *MNRAS*, 232, 35
- Wood, M. A., et al. 2005, *ApJ*, 634, 570
- Wood, M. A., & Burke, C. J. 2007, *ApJ*, 661, 1042
- Wood, J., Horne, K., Berriman, G., Wade, R., O'Donoghue, D., & Warner, B. 1986, *MNRAS*, 219, 629
- Wood, M. A., Montgomery, M. M., & Simpson, J. C. 2000, *ApJ*, 535, L39
- Wood, M. A., Thomas, D. M., & Simpson, J. C. 2009, *MNRAS*, 398, 2110
- Woudt, P. A., Warner, B., Osborne, J., & Page, K. 2009, *MNRAS*, 395, 2177
- Zhao, Y., Li, Z., Wu, X., Peng, Q., Zhang, Z., & Li, Z. 2006, *PASJ*, 58, 367